

EXPERIMENTAL VERIFICATION AND COMPARISON OF CONTROL
STRATEGIES FOR A SATELLITE MAGNETIC-BASED ATTITUDE CONTROL
SYSTEM UNDER A THREE-AXIS HELMHOLTZ CAGE ENVIRONMENT



THANAYUTH PANYALERT

A THESIS SUBMITTED IN PARTIAL FULFILLMENT
OF THE REQUIREMENT FOR THE DEGREE OF
MASTER OF ENGINEERING IN ROBOTICS AND COMPUTATIONAL INTELLIGENCE
SYSTEMS (MULTI-DISCIPLINARY PROGRAM)
SCHOOL OF ENGINEERING
KING MONGKUT'S INSTITUTE OF TECHNOLOGY LADKRABANG
2024
KMITL-2024-EN-M-070-232

This material is reserved for educational use only, not allowed for commercial use.

Forbidden to modify the content, and cite the document when use.



COPYRIGHT 2024

SCHOOL OF ENGINEERING

KING MONGKUT'S INSTITUTE OF TECHNOLOGY LADKRABANG

This material is reserved for educational use only, not allowed for commercial use.

Forbidden to modify the content, and cite the document when use.

Thesis	Experimental Verification and Comparison of Control Strategies for A Satellite Magnetic-Based Attitude Control System Under a Three-Axis Helmholtz Cage Environment
Student	Mr. Thanayuth Panyalert
Student ID.	63601257
Degree Program	Master of Engineering Robotics and Computational Intelligence Systems (Multi-Disciplinary Program)
Year	2024
Thesis Advisor	Asst.Prof.Dr.Poom Konghuayrob

ABSTRACT

In spacecraft mission planning and operation, the Attitude Determination and Control Subsystem (ADCS) of a satellite is crucial for determining its orientation in relation to the inertial reference frame and executing necessary adjustments, especially in Low-Earth Orbit (LEO). This study delves into the three-axis attitude control problem of the satellite, focusing on active and passive control methods such as de-tumbling control, magnetic control, and attitude stabilization after solar panel wing deployment using magnetorquers as the primary actuators. The goal is to stabilize the satellite and reduce angular rates while aligning it with the desired attitude. The proposed satellite Attitude Control System (ACS) strategies, including the B-dot control algorithm for de-tumbling and pointing algorithm for orientation, are designed, developed, characterized, and verified. Hardware-in-the-Loop simulation (HiLs) tests are conducted to evaluate the performance of the magnetic-based ACS in the presence of noise, utilizing a relative Earth's magnetic field (EMF) generator alongside SGP-4-based satellite orbital propagator high-level control software. Moreover, cascade Proportional-Integral-Derivative (PID) and state-dependent Riccati equation (SDRE) controllers are implemented to generate sufficient torque using three-axis magnetorquers on a frictionless air-bearing platform, with their performance evaluated using an on-board computer. Finally, the effectiveness of the co-simulation is validated as a primary experiment through an integrated HiLs process, confirming the control system's performance and its ability to meet mission requirements.

Acknowledgement

This thesis has been successfully completed with the excellent guidance of my advisor, Dr. Poom Konghuayrob. His assistance, guidance, and valuable knowledge significantly contributed to a positive learning experience for me.

I extend my sincere appreciation to Dr. Peerapong Torteeka, Khun Shariff Manuthasna, Khun Tanawish Masri, and Khun Jormpon Chaisakulsurin from the National Astronomical Research Institute of Thailand for their advice and suggestions on designing control systems, testing procedures, and conducting experiments.

I would like to express my special thanks to the National Research Council of Thailand for their financial support that facilitated the success of our research through the Hub of Talents in Spacecraft Scientific Payload, Grant No. N35E660131, and the Hub of Knowledge in Space Technology and its Application, Grant No. N35E660132. Additionally, I wish to acknowledge the School of Engineering, Department of Robotics and Artificial Intelligence, King Mongkut's Institute of Technology Ladkrabang, and the PBP CMU Electron Linac Laboratory (PCELL) at the Plasma and Beam Physics Research Facility of Chiang Mai University, Thailand. They provided advice and the measuring equipment used to validate the magnetic actuator in this experiment.

Thanayuth Panyalert

Table of Contents

	Page
English Abstract.....	I
Acknowledgement.....	II
Table of Contents.....	III
List of Tables.....	V
List of Figures.....	VI
Chapter 1 Introduction.....	1
1.1 Statement and Significance of The Problems.....	1
1.2 Goal and Objective.....	2
1.3 Scope or Limitation of The Study.....	2
1.4 Process of The Study.....	2
1.4.1 Satellite Model Description.....	3
1.4.2 Simulation Setup.....	3
1.4.3 Hardware-in-the-Loop (HiL) Setup.....	3
1.4.4 Control Method Evaluation.....	4
1.4.5 De-tumbling Phase.....	4
1.4.6 Solar Panel Wing Deployment.....	4
1.4.7 Normal-mode Operations.....	4
1.4.8 Analysis of Control Phases.....	4
Chapter 2 Literature Review.....	8
2.1 Satellite Attitude Representations.....	8
2.1.1 Direction Cosine Matrix.....	9
2.1.2 Euler Angles.....	9
2.1.3 Quaternion.....	10
2.2 Attitude Dynamics.....	12
2.3 Satellite Magnetic-Based Attitude Control System.....	13
2.3.1 De-tumbling along with Pointing Control using a Magnetorquer.....	15
2.4 Control Strategies.....	16
2.4.1 Cascade PID Control.....	16
2.4.2 SDRE Control.....	18
Chapter 3 Methodology.....	24
3.1 Configuration of the Hardware-in-the-Loop Simulation Platform	25
3.1.1 Three-Axis Helmholtz Cage.....	25
3.1.2 Magnetorquer Model.....	29
3.1.3 The Proposed HiLs Platform.....	31
Chapter 4 Experimental Results.....	36

This material is reserved for educational use only; not allowed for commercial use.

Forbidden to modify the content, and cite the document when use.

4.1 Experimental Results of De-tumbling along with Pointing Control.....	36
4.2 Experimental Results of Stabilization After the Deployment of Solar Panel Wings.....	39
4.3 Discussion.....	43
Chapter 5 Conclusion.....	45
References.....	47
Appendix Experimental Verification of Control Strategies for Satellite Magnetic-based Attitude Control System under A Three Axis Helmholtz Cage Environment.....	51



List of Tables

Table	Page
1.1 The process of Master's program studies.....	7
3.1 The HiLs testbed sub-system specification.....	26
3.2 Magnetorquer Parameters.....	28
3.3 The distance from the center of mass to the center of rotation, adjusted by the sliding masses on the satellite system model to align with the system's axis of rotation.....	33
4.1 The gain parameters for de-tumbling along with pointing control.....	36
4.2 Simulation parameters for HiLs	40
4.3 The evaluation of the de-tumbling along with pointing control performances.....	44
4.4 The evaluation of the stabilization control performances.....	44



List of Figures

Figure	Page
1.1 The satellite model.....	3
1.2 Earth Centered Inertial Frame, Body Frame and LVLH coordinate system.....	5
1.3 Satellite concept of operations.....	5
2.1 The orientation of the body frame with respect to the inertial frame.....	8
2.2 The proposed three orthogonal magnetorquers.....	14
2.3 The structure of the satellite attitude control system.....	15
2.4 The structure of the satellite attitude control system with a cascade PID controller.....	16
2.5 The structure of the satellite attitude control system with the SDRE controller.....	22
3.1 A system architecture of proposed HiLs testbed.....	25
3.2 Uniformity analysis of the proposed 3D square Helmholtz coil in a one-meter cubic-like area from the center. (a) The original data obtained from the calibrated magnetic sensor were visualized in a 3D surface plot, and (b) the radius of the ellipsoid represents the intensity of the magnetic field, with each transformed coordinate pointing away from the center of the origin.....	27
3.3 The magnetic field of the magnetorquer was measured using a Group3 DTM-130 digital teslameter with an LPT-130 probe and supplied power of 0V to 15V.....	29
3.4 (a) A 3D surface plot relationship between the measured magnetic field, and (b) the magnetic field intensity error of the magnetorquer.....	30
3.5 Linear approximation of the relationship between the generated magnetic moment and the applied voltage.....	30
3.6 The sliding masses for adjusting to balance the satellite system model	32
3.7 The number of iterations required to balance the center of mass to the center of rotation of the satellite system model.....	33
3.8 Block diagram of the HiLs platform.....	34
3.9 The components of the HiLs platform.....	34
4.1 The angular rate results of the HiLs test with the cascade PID + B-Dot controller.	38
4.2 The Euler angle results of the HiLs test with the cascade PID + B-Dot controller.....	39
4.3 The angular rate results of the HiLs test for stabilization after deployment of solar panel wings.	41

4.4 The Euler angle results of the HiLs test for stabilization after deployment of solar panel wings.....	42
4.5 The angular rate results with and without the controllers.....	43



Chapter 1

Introduction

1.1 Statement and Significance of The Problems

The Attitude Determination and Control Subsystem (ADCS) is a crucial element ensuring the stability and precision of satellites in delivering payloads to designated targets. It comprises two interconnected subsystems: the attitude determination system (ADS) and the attitude control system (ACS). The ADS utilizes sensors to ascertain the satellite's attitude or angular rates, while the ACS employs actuators, attitude control algorithms, and controllers to steer the satellite to a desired orientation [1]. The ADCS holds significant importance in satellite missions because it provides crucial attitude information and aids in stabilizing the satellite [2], [3], [4]. Among the various ACS actuators, the magnetorquer is particularly noteworthy. By generating a magnetic field that interacts with Earth's magnetic field (EMF), it proves to be a reliable strategy, especially in low Earth orbits [5]. During the satellite's transition from the de-tumbling phase, characterized by high angular rates, to the nominal mission, the ADCS must ensure the satellite's attitude remains controllable. This entails reducing the initial angular rate and achieving stabilization [6]. The hardware-in-the-loop simulation (HiLs) methodology presents an intriguing approach to test and validate guidance, navigation, and control software algorithms. It facilitates on-ground testing, allowing for a comprehensive assessment and verification of software performance.

The HiLs configuration incorporates several essential elements. Initially, a Helmholtz cage is employed to precisely replicate the EMF vector, replicating the effects encountered by the satellite during orbital motion. Furthermore, a simulation loop integrates a magnetometer to offer real-time feedback, while an air-bearing platform enables almost frictionless rotational motion. This setup facilitates the simulation of satellite attitude dynamics under the control of a magnetorquer-based ACS [7], [8], [9], [10]. The utilization of a HiLs for satellite process verification offers numerous benefits, including resource, time, and cost savings. By conducting simulations using HiL technology, designers can obtain valuable insights into potential causes of failure and make necessary adjustments to the control algorithm [11]. This iterative process enables continuous improvement and refinement of a satellite's attitude control system. Research on satellite ACS has become trending topic in recent years [12]. The controllers of linear strategies, such as the PD controller, are widely used in ACS due to their simple structure and good stability [13], [14]. The LQR

This material is reserved for educational use only, not allowed for commercial use.

controller stabilizes a three-axis satellite [15], [16], and the satellite ACS using magnetic torquers has been simulated under two different inertia conditions (after and before the boom extension) [17]. Various software-in-the-loop control techniques have been developed. Nonetheless, ground testing, including HiLs, remains essential for the ongoing enhancement of the ACS system's performance [7], [18]. Therefore, the verification and validation of control strategies through ground-based testing via HiLs are crucial to guarantee that the developed ACS can effectively stabilize the satellite after deployment.

1.2 Goal and Objective

This study primarily aims to validate the efficacy of the control algorithm assessed via HiLs, employing a three-axis magnetorquer to de-tumble the satellite model during the de-tumbling phase scenario. Furthermore, it seeks to verify the performance of both the cascade PID controller and the SDRE controller. Additionally, the SDRE controller is utilized to stabilize the solar panel wings after deployment. The performance of both controllers is then verified using an onboard computer. The objectives include:

- Design and construct a three-axis magnetorquer.
- Design ACS for de-tumbling along with pointing to the desired attitude and stabilize the solar panel wings after deployment using a three axis magnetorquer.
- Develop ACS with the B-dot algorithm and the cascade PID controller and the SDRE in MATLAB.
- Verify ACS through the HiLs.

1.3 Scope or Limitation of The Study

- Design and construct the satellite model based on the microsatellite type with a mass range of 10-100 kg.
- The proposed three-axis magnetorquer and satellite model will be tested and validated only through ground-based HiLs.
- The control strategies will be designed for de-tumbling during the de-tumbling phase and for attitude stabilization after solar panel wing deployment.

1.4 Process of The Study

To validate and verify the performance of the various control methods, a comprehensive simulation-based approach is employed. The satellite model, which serves as the control object in this project, undergoes simulated testing under identical conditions. The methodology involves the following steps:

This material is reserved for educational use only, not allowed for commercial use.

Forbidden to modify the content, and cite the document when use.

1.4.1 SATELLITE MODEL DESCRIPTION

The satellite model utilized in this study weighs 17.7 kg and measures 200×200×200 mm undeployed, as shown in Figure 1.1. It functions as a three-axis stabilized satellite, utilizing a magnetic controller for de-tumbling and pointing control, along with attitude stabilization after solar panel wing deployment. Attitude control is managed by three magnetorquers, oriented along the nominal principal body axes. Additionally, the satellite model includes a movable simulated mass in the form of solar panel wings designed to simulate changes in the inertia tensor during the deployment of the solar panel wings.

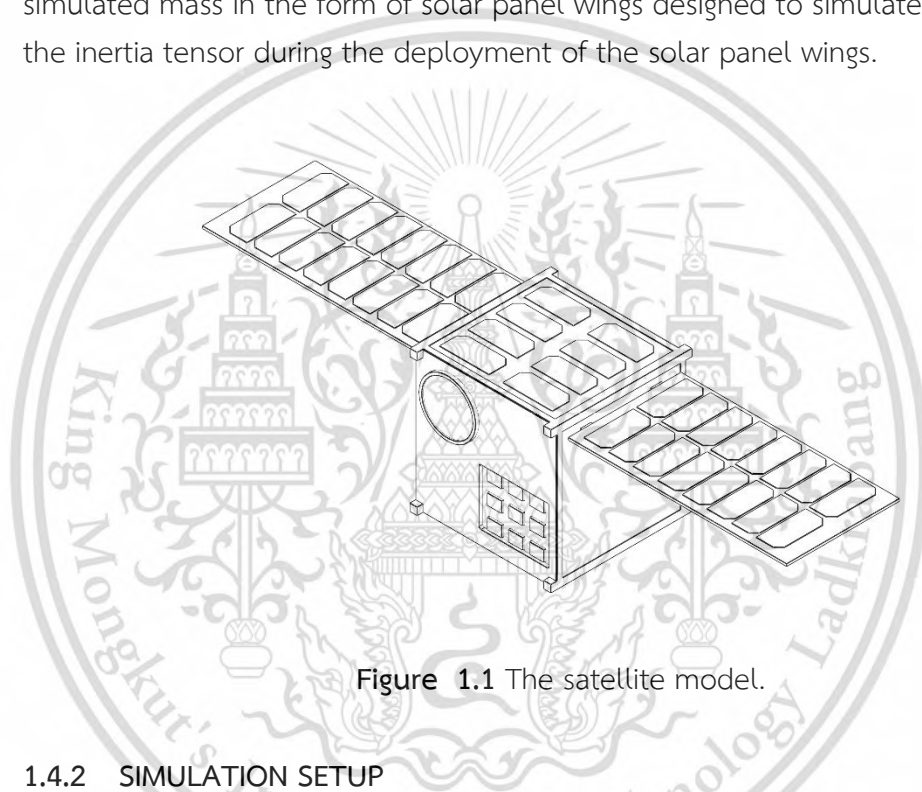


Figure 1.1 The satellite model.

1.4.2 SIMULATION SETUP

The simulations are conducted using MATLAB software, ensuring accurate representation of the satellite dynamics and control system behavior. Identical initial conditions are set for each control method simulation to enable fair comparison of their performance.

1.4.3 HARDWARE-IN-THE-LOOP (HIL) TESTING

HiL testing is employed to validate the control algorithms in a hardware environment, bridging the gap between simulation and real-world implementation. A hardware setup consisting of physical components such as actuators, sensors, and a control interface is interfaced with the simulation software. The control algorithms developed within the simulation environment are implemented, controlling the hardware components and interacting with the

This material is reserved for educational use only, not allowed for commercial use.

Forbidden to modify the content, and cite the document when use.

simulated satellite model. HiL testing allows for assessment of the control methods' performance under hardware conditions, providing valuable insights into their effectiveness.

1.4.4 CONTROL METHODS EVALUATION

Various control methods, including the cascade PID and SDRE controllers, are implemented and evaluated in both the simulation environment and the HiL setup. Performance metrics such as de-tumbling time and attitude accuracy are used to assess the effectiveness of each control method in both simulation and HiLs testing.

1.4.5 DE-TUMBLING PHASE

The initial phase of the HiLs testing focuses on de-tumbling the satellite after separation from the launcher. Control methods are applied to reduce the satellite's rotational rates to a sufficiently low level, preparing for solar panel wing deployment [3].

1.4.6 SOLAR PANEL WING DEPLOYMENT

Upon reaching the desired rotational rates, the solar panel wings are deployed, initiating passive attitude stabilization through the nonholonomic motion planning effect [19]. The deployment process and its impact on the satellite's dynamics are closely monitored and analyzed in HiLs testing.

1.4.7 NORMAL-MODE OPERATIONS

Following successful de-tumbling and solar panel deployment, the satellite enters normal-mode operations. Control methods are employed to maneuver the satellite into the local vertical local horizontal system (LVLH), representing an Earth-pointing attitude, as depicted in Figure 1.2. The concept of the control phases is illustrated in Figure 1.3.

1.4.8 ANALYSIS OF CONTROL PHASES

The effectiveness of each control method during different phases of the mission is analyzed and compared, leveraging insights from HiLs testing. Results are interpreted to gain a comprehensive understanding of the performance and suitability of the control methods for the satellite's mission objectives.

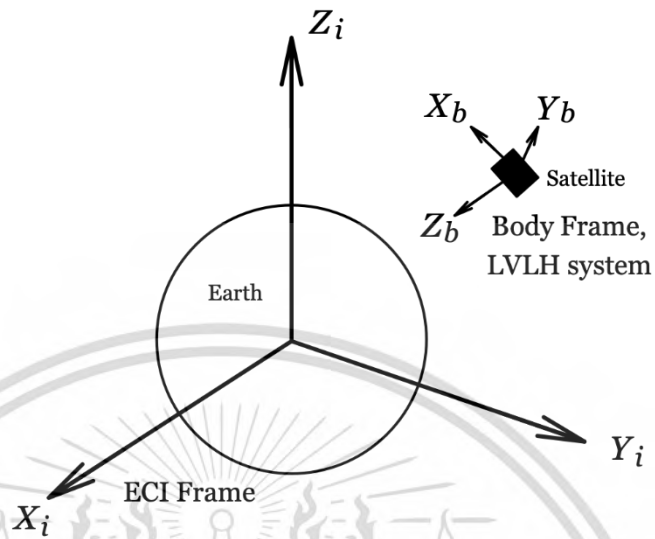


Figure 1.2 Earth Centered Inertial Frame, Body Frame and LVLH coordinate system.

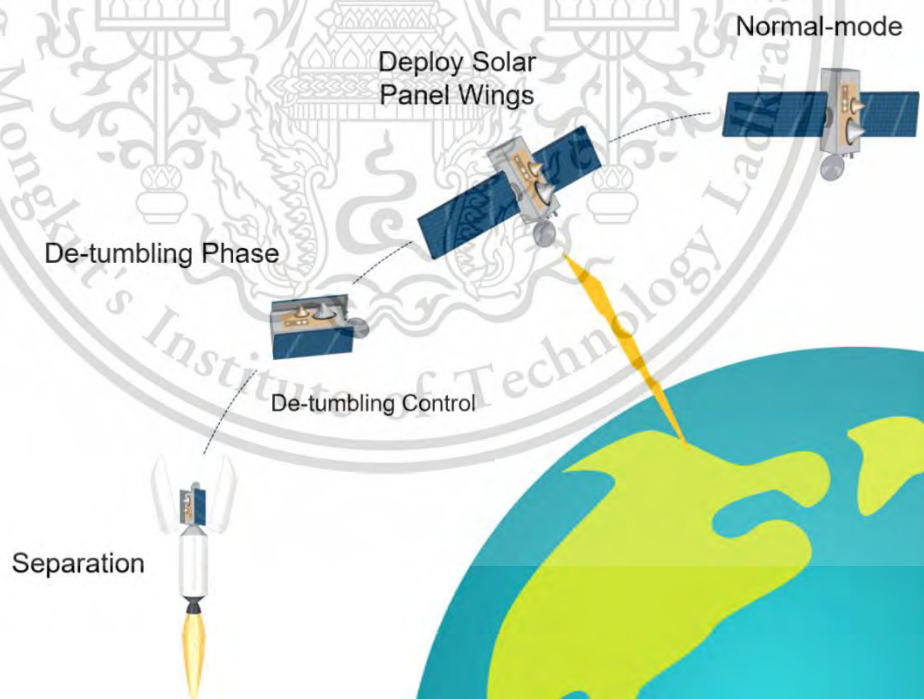


Figure 1.3 Satellite concept of operations.

By integrating HiLs testing into the validation and verification process, the study aims to provide robust and reliable assessments of the control methods' performance, facilitating their real-world implementation in satellite missions.



This material is reserved for educational use only, not allowed for commercial use.

Forbidden to modify the content, and cite the document when use.

Chapter 2

Literature Review

2.1 Satellite Attitude Representations

The satellite attitude representation is defined as a set of 3x3 rotation matrices that describe the rigid body orientation of an initial reference frame with respect to a second reference frame. However, many attitude representations can be used to define the satellite's orientation, and some of the common representations used in this task are summarized below. Figure 2.1 shows the orientation of the body frame with respect to the inertial frame.

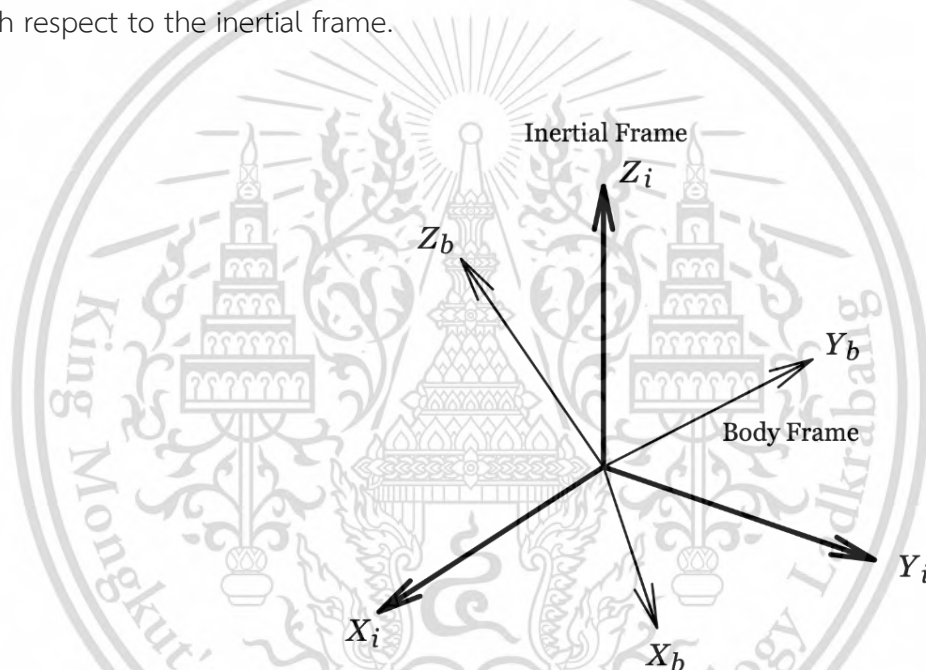


Figure 2.1 The orientation of the body frame with respect to the inertial frame.

The paper will utilize the following reference systems for describing satellite attitude:

- Inertial Coordinate Frame: The inertial frame has its origin at the center of the Earth. The Z_i -axis is perpendicular to the Earth's equatorial plane, pointing towards the arctic. The X_i -axis lying in the Earth's equatorial plane, pointing in the direction of the vernal equinox. This coordinate frame follows a right-handed orientation with the Y_i -axis.
- Orbit Coordinate Frame: The orbit frame originates at the satellite's center of mass. The Z_o -axis points towards the center of the Earth, while the X_o -axis

This material is reserved for educational use only, not allowed for commercial use.

Forbidden to modify the content, and cite the document when use.

lying in the orbit plane perpendicular to the Z_o -axis, pointing in the direction of the satellite's velocity. This coordinate frame is right-handed, with the Y_o -axis completing the orientation.

- **Satellite Body Frame:** The body frame is defined with its origin at the satellite's center of mass, and the axes (X_b, Y_b, Z_b) coincide with the body's principal inertia axes. The body frame aligns with the orbit frame when the spacecraft is three-axis stabilized in an Earth-pointing attitude scenario.

Figure 1.2 displays the representations of the satellite body frames and the LVLH frames used in this paper to represent the orbit-referenced frames. In the nadir-pointed attitude configuration, the satellite body frame aligns with the LVLH frame. The Z-axis of the LVLH frame points toward the Earth's center, the Y-axis aligns with the orbit, and the X-axis is positioned in the orbit-plane perpendicular to Z and directed along the velocity vector.

2.1.1 DIRECTION COSINE MATRIX

The direction cosine matrix (DCM) is a mathematical parameter representing the attitude orientation of a three-dimensional body. The parameters are utilized as the three-axis attitude transformation value that describes the direction of the fixed frame to the body frame. The Euler angle rotation yaw-pitch-roll sequence is used to describe this satellite's orientation [20], as shown in the following direction cosine matrix in Equation (2.1):

$$[C_{123}] = \begin{bmatrix} c\theta c\psi & c\theta s\psi & -s\theta \\ -c\phi s\psi + s\phi s\theta c\psi & c\phi c\psi + s\phi s\theta s\psi & s\phi c\theta \\ s\phi s\psi + c\phi s\theta c\psi & -s\phi c\psi + c\phi s\theta s\psi & c\phi c\theta \end{bmatrix} \quad (2.1)$$

2.1.2 EULER ANGLES

The satellite's orientation with respect to the fixed frame can be described by a three-coordinate rotation sequence. Each rotation is a single axis in the body frame. The satellite's attitude is represented using three coordinate rotations known as the Euler angles [3]. However, considering the set of Euler angles corresponding to yaw-pitch-roll, the three single-axis rotation matrices $[M_i(\theta)]$ be defined as

$$\begin{aligned}
[M_1(\theta)] &= \begin{bmatrix} 1 & 0 & 0 \\ 0 & \cos\theta & \sin\theta \\ 0 & -\sin\theta & \cos\theta \end{bmatrix}, \\
[M_2(\theta)] &= \begin{bmatrix} \cos\theta & 0 & -\sin\theta \\ 0 & 1 & 0 \\ \sin\theta & 0 & \cos\theta \end{bmatrix}, \\
[M_3(\theta)] &= \begin{bmatrix} \cos\theta & c\theta s\psi & 0 \\ -\sin\theta & \cos\theta & 0 \\ 0 & 0 & 1 \end{bmatrix}.
\end{aligned} \tag{2.2}$$

Let the Euler angles sequence be $(\theta_1, \theta_2, \theta_3) = (\psi, \theta, \phi)$ and combine successive coordinate rotation

$$[C(\theta_1, \theta_2, \theta_3)] = [C(\psi, \theta, \phi)] = [M_1(\psi)M_2(\theta)M_3(\phi)]. \tag{2.3}$$

The direction cosine matrix in terms of the yaw-pitch-roll Euler angles (3-2-1) can be written as Equation (2.1).

2.1.3 QUATERNION

A quaternion is a four-dimensional vector attitude representation by four variables compared to three variables in Euler angles. This single four-element model consists of a scalar term q_0 and \vec{q} a vector term [21]. Quaternions can be considered in the following way:

$$q = q_0 + q_1i + q_2j + q_3k \tag{2.4}$$

where $q = (q_0, \vec{q})$, q_0 is the scalar part, $\vec{q} = (q_1, q_2, q_3)$ is the vector part and i , j and k are the unit vectors of the quaternion. The unit vectors are described below:

$$\begin{aligned}
i^2 &= j^2 = k^2 = ijk = -1, \\
ij &= k, & ji &= -k, \\
jk &= i, & kj &= -i, \\
ki &= j, & ik &= -j.
\end{aligned} \tag{2.5}$$

The Euler angle is easily determined by transforming to the quaternion using a two-step process. The quaternion is first transformed into a DCM. The DCM element can be expressed in the associated quaternion [21]:

$$C_q = \begin{bmatrix} q_0^2 + q_1^2 - q_2^2 - q_3^2 & 2(q_1q_2 + q_0q_3) & 2(q_1q_3 - q_0q_2) \\ 2(q_1q_2 - q_0q_3) & q_0^2 - q_1^2 + q_2^2 - q_3^2 & 2(q_2q_3 + q_0q_1) \\ 2(q_1q_3 + q_0q_2) & 2(q_2q_3 - q_0q_1) & q_0^2 - q_1^2 - q_2^2 + q_3^2 \end{bmatrix}. \quad (2.6)$$

Equation (2.6) can easily be obtained as

$$C_q = \begin{bmatrix} c_{11} & c_{12} & c_{13} \\ c_{21} & c_{22} & c_{23} \\ c_{31} & c_{32} & c_{33} \end{bmatrix}. \quad (2.7)$$

Then, the set of Euler angles is extracted from the DCM Equation (2.6) depending on the Euler angle sequence. The Euler angles (3-2-1) yaw-pitch-roll can be converted from the DCM with the following transformation:

$$\begin{aligned} \psi &= \tan^{-1} \frac{c_{12}}{c_{11}}, \\ \theta &= -\sin^{-1} c_{13}, \\ \phi &= \tan^{-1} \frac{c_{22}}{c_{33}}. \end{aligned} \quad (2.8)$$

Similarly, a quaternion can be determined from a set of Euler angles using a two-step transformation. The set of Euler angles is first transformed into a DCM using Equation (2.1), and then the quaternion can be found from the elements of the DCM. The squares of each quaternion term are calculated using the following numerical method [21]:

$$\begin{aligned} q_0^2 &= \frac{1}{4}(1 + c_{11} + c_{22} + c_{33}), \\ q_1^2 &= \frac{1}{4}(1 + c_{11} - c_{22} - c_{33}), \\ q_2^2 &= \frac{1}{4}(1 - c_{11} + c_{22} - c_{33}), \\ q_3^2 &= \frac{1}{4}(1 + c_{11} - c_{22} - c_{33}). \end{aligned} \quad (2.9)$$

One of the quaternions can be calculated using Equation (2.9) by taking the square root of the maximum value terms. The other quaternion terms can be computed using Equation (2.10) [22] as follows:

$$q = \frac{1}{4q_0} \begin{bmatrix} c_{23} - c_{32} \\ c_{31} - c_{13} \\ c_{12} - c_{21} \\ 4q_0^2 \end{bmatrix} = \frac{1}{4q_1} \begin{bmatrix} 4q_1^2 \\ c_{12} + c_{21} \\ c_{31} + c_{13} \\ c_{23} - c_{32} \end{bmatrix} = \frac{1}{4q_2} \begin{bmatrix} c_{12} + c_{21} \\ 4q_2^2 \\ c_{23} + c_{32} \\ c_{31} - c_{13} \end{bmatrix} = \frac{1}{4q_3} \begin{bmatrix} c_{31} - c_{13} \\ c_{23} + c_{32} \\ 4q_3^2 \\ c_{12} - c_{21} \end{bmatrix}. \quad (2.10)$$

2.2 Attitude Dynamics

A satellite attitude control system refers to the system or set of components and algorithms designed to control and manipulate the orientation or attitude of a satellite. Attitude control involves changing the satellite's angular position, velocity, or orientation in space to achieve specific mission objectives, such as pointing instruments, maintaining stability, or adjusting orbital parameters. The satellite attitude control system plays a crucial role in tasks such as satellite pointing, stabilization, orbital maneuvers, attitude synchronization, and precision control during scientific observations or payload operations. The magnetic attitude dynamics are modeled by considering the satellite's rotational behavior when magnetic actuation is employed. The satellite is regarded as a rigid body capable of rotating around its center of mass. Euler angles are utilized to convert the body frame into an inertial reference frame to describe the satellite's attitude. The angular rate of the satellite, represented in the body frame, corresponds to its rotation relative to the inertial reference frame. Euler's equation is employed to approximate the dynamic equation of the satellite as follows [2]:

$$I\dot{\omega} = -\omega \times I\omega + \tau \quad (2.11)$$

where $\tau = (\tau_x, \tau_y, \tau_z)^T$ represents the torque vector expressed in the satellite body frame, $\omega = (\omega_x, \omega_y, \omega_z)^T$ denotes the angular rate, and I denotes the moment of inertia matrix of the satellite body frame. Based on magnetic actuation, such as through magnetorquers, Equation (2.12) can then be modified as follows:

$$I\dot{\omega} = -\omega \times I\omega + \tau_{mtq} + \tau_{dist} \quad (2.12)$$

where τ_{mtq} represents the vector of magnetic torques generated by the magnetorquers, and τ_{dist} denotes the vector of external disturbance torques [2].

2.3 Satellite Magnetic-Based Attitude Control System

A magnetorquer serves as an actuator for controlling the satellite attitude. It generates a magnetic dipole moment, represented as $\mathbf{m} = (m_x, m_y, m_z)^T$, from the coil component. This magnetic dipole moment interacts with the EMF, generating torque that enables control over the satellite's orientation. The strength of the dipole moment is regulated by the magnitude of the current. The control torque generated by the magnetorquers can be described as [2]:

$$\tau_{mtq} = \mathbf{m} \times \mathbf{b}(t) \quad (2.13)$$

$$\mathbf{b}(t) = \mathbf{C}_q \cdot \mathbf{b}_0(t) \quad (2.14)$$

where $\mathbf{b} = (b_x, b_y, b_z)^T$ represents the magnetic field in the body frame, expressed relative to the attitude matrix \mathbf{C}_q and the magnetic field vector expressed in the ECI coordinates $\mathbf{b}_0(t)$.

The proposed three-axis square air-core magnetorquers have been specifically designed for utilization in this project. Figure 2.2 illustrates the three orthogonal magnetorquers, which necessitate independent control along their respective axes. Equation (2.14) represents the magnetic moment associated with each air-core magnetorquer as follows:

$$\mathbf{m} = i \cdot \mathbf{n} \cdot \mathbf{S} \quad (2.14)$$

where i represents the current, \mathbf{n} stands for the number of windings in the coil and \mathbf{S} denotes the area enclosed by a turn of the coil's spiral.

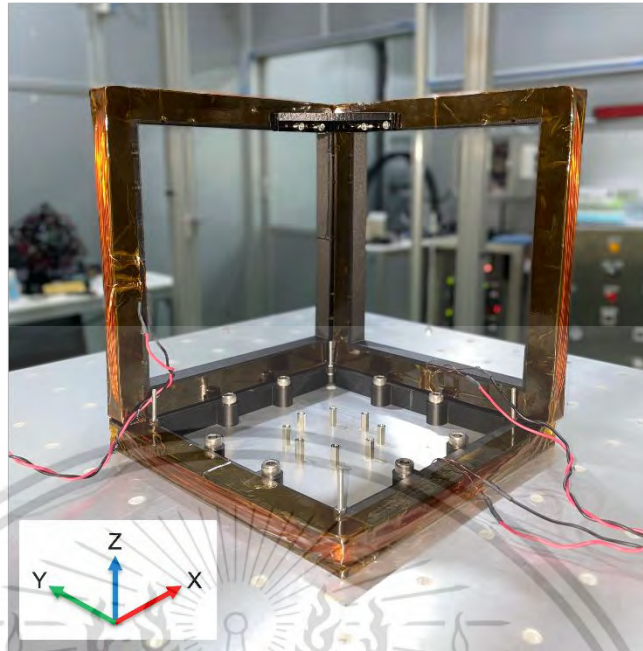


Figure 2.2 The proposed three orthogonal magnetorquers.

To ensure the accuracy of the magnetorquers, the percentage difference in the magnetic field intensity is assessed by comparing the calculated magnetic field intensity with the measured values. This verification process serves to confirm the reliability and precision of the magnetorquers. The magnetic field intensity of the magnetorquer, denoted as m_{mtq} , is computed using Biot-Savart's law [23], as depicted in Equation (2.15), and the percentage difference of the magnetic field intensity, denoted as $\%error$, can be defined as

$$b_{mtq}(z) = \frac{2\mu_0 n i a_{sq}^2}{\pi} \left[(a_{sq}^2 + z^2)^{-1} (2a_{sq}^2 + z^2)^{-\frac{1}{2}} \right], \quad (2.15)$$

$$\%error = \frac{b_{mtq} - b_{mea}}{b_{mea}} \times 100. \quad (2.16)$$

In Equation (2.15), the variable z represents the distance from the measurement point along the z -axis. The magnetic constant is denoted as $\mu_0 = 4\pi \times 10^{-7}$ H/m, and a_{sq}^2 represents the half length of the square coil. The magnetic dipole moment from this verification can be computed using Equation (2.17) below:

$$m_{mea} = \frac{4b_{mea}(z)\pi}{2\mu_0} \left[(a_{sq}^2 + z^2)^1 (2a_{sq}^2 + z^2)^{\frac{1}{2}} \right]. \quad (2.17)$$

This material is reserved for educational use only, not allowed for commercial use.

Forbidden to modify the content, and cite the document when use.

Here, m_{mea} represents the measured magnetic dipole moment of the magnetorquer. The closed-loop satellite magnetorquer-based attitude control system comprises magnetorquers, attitude sensors, an attitude controller, and a satellite model, as depicted in Figure 2.3.

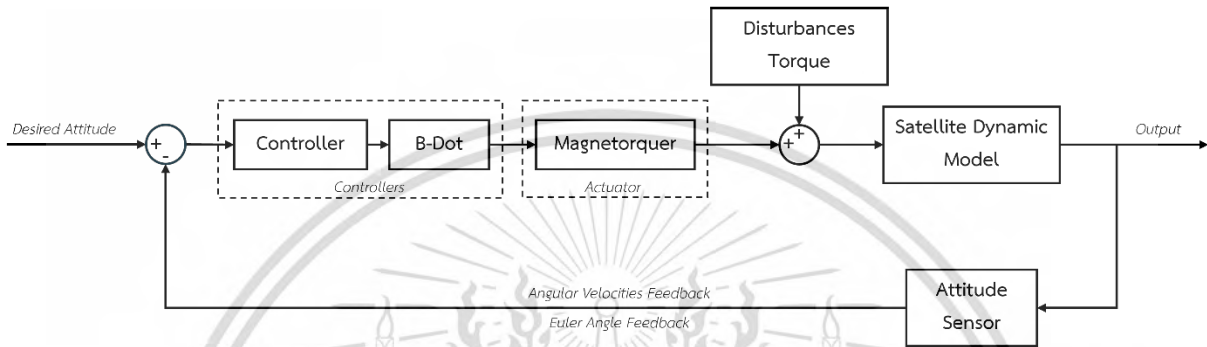


Figure 2.3 The structure of the satellite attitude control system.

2.3.1 DE-TUMBLING ALONG WITH POINTING CONTROL USING A MAGNETORQUER

To reduce the angular rate, a de-tumbling controller is necessary. The B-dot controller, which is a widely used control law for de-tumbling satellites, was selected for this project due to its performance near the required attitude [24], recognized effectiveness, simplicity, and widespread adoption [21], [25]. The B-dot controller is mathematically represented by Equations (2.18)-(2.19) as follows:

$$\dot{\mathbf{b}} \approx \mathbf{b} \times \boldsymbol{\omega}. \quad (2.18)$$

$$\mathbf{m}_b = \frac{-k_b}{\|\mathbf{b}\|} \dot{\mathbf{b}} \quad (2.19)$$

$\dot{\mathbf{b}}$ corresponds to the time derivative of the measured magnetic field in the body frame with opposite signs. The approximation of $\dot{\mathbf{b}}$ can be obtained using the equation specified in Equation (2.18) [25], [26], \mathbf{m}_b in Equation (2.19) represents the vector of the commanded magnetic dipole moment generated by the magnetorquers, k_b denotes a positive definite gain matrix.

For this project, the de-tumbling and pointing control algorithm will be implemented in MATLAB to assess the performance of the satellite magnetic-based ACS. Subsequently, the control strategies will be incorporated, and the experimental results section will validate the effectiveness of the implemented algorithms.

2.4 Control Strategies

The control strategies implemented in this task, including the use of cascade proportional-integral-derivative (PID) and state-dependent Riccati equation (SDRE) controllers, are presented in this subsection. These controllers are used to generate sufficient torque using the three-axis magnetorquers of the satellite model to interact with the EMF simulation to stabilize and reach the desired attitude.

2.4.1 CASCADE PID CONTROL

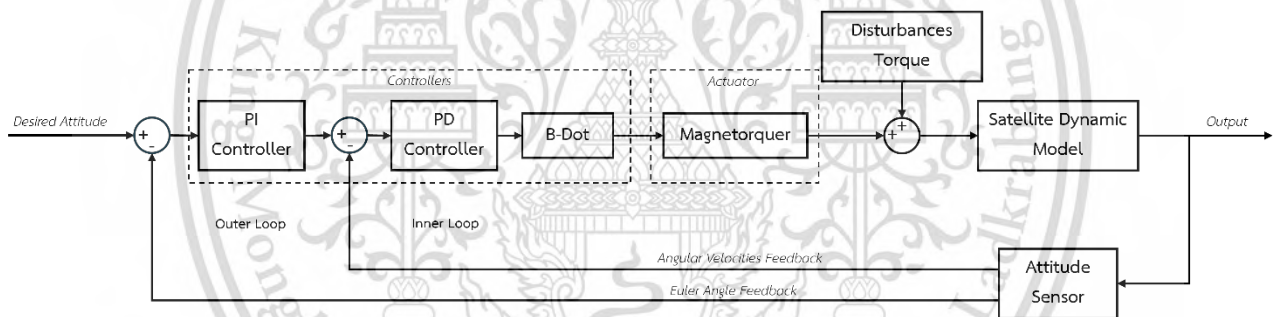


Figure 2.4 The structure of the satellite attitude control system with a cascade PID controller

The satellite magnetic-based ACS operates in a closed-loop configuration, incorporating magnetorquers, attitude sensors, an attitude controller, and a satellite model. For this study, a cascade PID controller is devised to regulate the attitude of the satellite model. The structure of the satellite attitude control system, incorporating the cascade PID controller, is presented in Figure 2.4. The discrete-time form of the PID controller is expressed by Equation (2.20) [27]:

$$u(k) = u(k-1) + \left(K_p + K_i \frac{T}{2} + \frac{K_d}{T} \right) e(k) + \left(-K_p + K_i \frac{T}{2} - \frac{K_d}{T} \right) e(k-1) + \frac{K_d}{T} e(k-2) \quad (2.20)$$

where $e(k) = r(k) - y(k)$ is the system error, K_p is the proportional gain, K_i is the integral gain, K_d is the derivative gain, k is the sampling index and T is a sampling period.

A cascade PID controller is employed in this task, incorporating two distinct control loops to achieve effective control over the satellite's attitude. The cascade control strategy is beneficial in systems where different aspects of the process need to be controlled with varying dynamics and precision.

- Inner Loop, Primary PD Controller:** The inner loop is dedicated to the fast dynamics of the system, specifically the regulation of the satellite's angular rate. This loop utilizes a Proportional-Derivative (PD) controller. The PD controller's primary function is to stabilize the satellite's angular velocity by applying immediate corrections based on the rate of change of the error (derivative term) and the current error (proportional term). This ensures that any deviations in the angular rate are promptly corrected, providing a quick response to disturbances and enhancing the overall stability of the system.
- Outer Loop, Secondary PI Controller:** The outer loop addresses the slower dynamics of the system, focusing on the control of the satellite's attitude in terms of Euler angles (roll, pitch, and yaw). This loop employs a Proportional-Integral (PI) controller. The PI controller aims to minimize the error in the satellite's attitude by integrating the error over time (integral term) and reacting to the current error (proportional term). The integral component is crucial for eliminating steady-state errors, ensuring that the satellite achieves and maintains the desired orientation accurately.

The output of the outer loop's PI controller, which represents the desired angular rate (reference signal for angular velocity), is fed into the inner loop as the reference signal (r_{vel}). This hierarchical control structure allows the outer loop to set the overall orientation objectives, while the inner loop manages the rapid adjustments needed to follow the given trajectory. Mathematically, the reference signal for the inner loop r_{vel} is derived from the PI controller in the outer loop, as shown in Equation (2.21). This integration ensures a coordinated control effort where the outer loop's objective of minimizing Euler angle errors is effectively translated into precise angular rate commands handled by the inner loop. Figure 2.4 illustrates this cascade PID control setup, showing the satellite model along with both the inner PD and outer PI controllers. The diagram

provides a clear visualization of how the two control loops interact and contribute to the overall control strategy.

$$r_{vel}(k) = r_{vel}(k-1) + \left(K_{p,ang} + K_{i,ang} \frac{T}{2}\right) e_{ang}(k) + \left(-K_{p,ang} + K_{i,ang} \frac{T}{2}\right) e_{ang}(k-1) \quad (2.21)$$

The primary goal of the PI controller in the outer loop is to reduce the error in the Euler angles (e_{ang}). By continually adjusting the control inputs based on the accumulated error and the current deviation, the PI controller ensures that the satellite's attitude converges to the desired setpoints, providing accurate and stable orientation control. The system error of the Euler angles is represented by $e_{ang}(k) = r_{ang}(k) - y_{ang}(k)$, where $r_{ang}(k)$ denotes the desired Euler angles and $y_{ang}(k)$ represents the measured Euler angles. The PD controller is responsible for adjusting the angular rate. Importantly, a relationship exists between the angular rate and the Euler angles. Modifying the angular rate induces changes in the Euler angles, which are interdependent. Consequently, controlling the angular rate entails manipulating the Euler angles to achieve the desired attitude. The control signals u_{sat} of the satellite magnetic-based ACS, incorporating the cascade PID controller, are determined using Equation (2.22) as follows:

$$u_{sat}(k) = u_{sat}(k-1) + \left(K_{p,vel} + \frac{K_{d,vel}}{T}\right) e_{vel}(k) + \left(-K_{p,vel} - \frac{K_{d,vel}}{T}\right) e_{vel}(k-1) + \frac{K_{d,vel}}{T} e_{vel}(k-2) \quad (2.22)$$

where $e_{vel}(k) = r_{vel}(k) - y_{vel}(k)$ is the angular rate system error, where $y_{vel}(k)$ represents the measured angular rate. The control signal is defined to adjust the angular rate, $\omega_{error} = 0 - u_{sat}$, which is then used to calculate the time derivative of the measured magnetic field in the body frame in Equation (2.18) for estimating the commanded magnetic dipole moment. This moment is generated by the magnetorquers, supplying enough electric current, as determined by Equation (2.19).

2.4.2 SDRE CONTROL

Over the past decade, state-dependent Riccati equation (SDRE) control has gained widespread recognition and popularity. It presents a highly effective

This material is reserved for educational use only, not allowed for commercial use.

Forbidden to modify the content, and cite the document when use.

algorithm for synthesizing nonlinear feedback controls, accommodating nonlinearities in the system states, and providing substantial design flexibility through state-dependent weighting matrices [28]. This paper focuses on employing an SDRE nonlinear regulator to address nonlinear optimal control problems related to the magnetorquer-based attitude model of a satellite, specifically for de-tumbling along with pointing control and stabilization of solar panel wing deployment. The mathematical representation of the magnetorquer-based attitude model of a satellite, discussed herein, is nonlinear and can be expressed by Equation (2.23).

$$\begin{aligned}
 \dot{\phi} &= \omega_x + \sin\phi \tan\theta \omega_y + \cos\phi \tan\theta \omega_z \\
 \dot{\theta} &= \cos\theta \omega_y - \sin\theta \omega_z \\
 \dot{\psi} &= \frac{\sin\phi \omega_y - \cos\phi \omega_z}{\cos\theta} \\
 \dot{\omega}_x &= \frac{(I_y - I_z)}{I_x} \omega_y \omega_z + \frac{\tau_x}{I_x} \\
 \dot{\omega}_y &= \frac{(I_z - I_x)}{I_y} \omega_x \omega_z + \frac{\tau_y}{I_y} \\
 \dot{\omega}_z &= \frac{(I_x - I_y)}{I_z} \omega_x \omega_y + \frac{\tau_z}{I_z}
 \end{aligned} \tag{2.23}$$

The state-space model of discrete-time system satellite dynamics can be expressed with Equation (2.24) [29] as follows:

$$\begin{aligned}
 x(t+1) &= Ax(t) + Bu(t), \\
 y(t) &= Cx(t) + Du(t)
 \end{aligned} \tag{2.24}$$

where the state vector x is defined as $(\psi, \theta, \phi, \omega_x, \omega_y, \omega_z)^T$, the control torque u is defined as $(\tau_x, \tau_y, \tau_z)^T$, A is the state matrix, B is the input matrix and C is the output matrix. The linearity of the system is crucial for establishing a linear time-invariant (LTI) system. Linearization of the system can be attained by calculating the Jacobian matrix, as exemplified by the following equation:

$$J_{i,j} = \frac{\partial f_i}{\partial x_j} = \begin{bmatrix} \frac{\partial f_1}{\partial x_1} & \frac{\partial f_1}{\partial x_2} & \dots & \frac{\partial f_1}{\partial x_6} \\ \frac{\partial f_2}{\partial x_1} & \frac{\partial f_2}{\partial x_2} & \dots & \frac{\partial f_2}{\partial x_6} \\ \vdots & \vdots & \ddots & \vdots \\ \frac{\partial f_6}{\partial x_1} & \frac{\partial f_6}{\partial x_2} & \dots & \frac{\partial f_6}{\partial x_6} \end{bmatrix} \tag{2.25}$$

This material is reserved for educational use only, not allowed for commercial use.

Forbidden to modify the content, and cite the document when use.

Therefore, the comprehensive linearized system of the satellite attitude model can be expressed as Equation (2.26).

$$A_{i,j} = \begin{bmatrix} A_{1,1} & A_{1,2} & \cdots & A_{6,1} \\ A_{2,1} & A_{2,2} & \cdots & A_{6,2} \\ \vdots & \vdots & \ddots & \vdots \\ A_{6,1} & A_{6,2} & \cdots & A_{6,6} \end{bmatrix}$$

$$B = \begin{bmatrix} \frac{1}{I_x} & 0 & 0 \\ 0 & \frac{1}{I_y} & 0 \\ 0 & 0 & \frac{1}{I_z} \end{bmatrix}, \quad C = \begin{bmatrix} 0 & 0 & 0 & 1 & 0 & 0 \\ 0 & 0 & 0 & 0 & 1 & 0 \\ 0 & 0 & 0 & 0 & 0 & 1 \end{bmatrix} \quad (2.26)$$

where

$$A_{1,1} = \omega_y \cos\phi \tan\theta - \omega_z \tan\theta \sin\phi$$

$$A_{1,2} = \omega_z \cos\phi (\tan^2\theta + 1) + \omega_y \sin\phi (\tan^2\theta + 1)$$

$$A_{1,3} = 0$$

$$A_{1,4} = 1$$

$$A_{1,5} = \tan\theta \sin\phi$$

$$A_{1,6} = \cos\phi \tan\theta$$

$$A_{2,1} = -\omega_z \cos\phi - \omega_y \sin\phi$$

$$A_{2,2}, A_{2,3}, A_{2,4} = 0$$

$$A_{2,5} = \cos\phi$$

$$A_{2,6} = -\sin\phi$$

$$A_{3,1} = \frac{\omega_y \cos\phi + \omega_z \sin\phi}{\cos\theta}$$

$$A_{3,2} = -\frac{\sin\theta (\omega_z \cos\phi - \omega_y \sin\phi)}{\cos^2\theta}$$

$$A_{3,3}, A_{3,4} = 0$$

$$A_{3,5} = \frac{\sin\phi}{\cos\theta}$$

$$A_{3,6} = -\frac{\cos\phi}{\cos\theta}$$

$$A_{4,1}, A_{4,2}, A_{4,3}, A_{4,4} = 0$$

$$A_{4,5} = \frac{\omega_z (I_y - I_z)}{I_x}$$

$$A_{4,6} = \frac{\omega_y (I_y - I_z)}{I_x}$$

$$A_{5,1}, A_{5,2}, A_{5,3}, A_{5,5} = 0$$

$$A_{5,4} = -\frac{\omega_z(I_x - I_z)}{I_y}$$

$$A_{5,6} = -\frac{\omega_x(I_x - I_z)}{I_y}$$

$$A_{6,1}, A_{6,2}, A_{6,3}, A_{6,6} = 0$$

$$A_{6,4} = \frac{\omega_y(I_x - I_y)}{I_z}$$

$$A_{6,5} = \frac{\omega_x(I_x - I_y)}{I_z}$$

Controllability and observability are vital concepts within the realm of the state space representation of a system, a subject integral to control systems [30]. For a dynamic system to respond as desired under control inputs, it must be controllable. Similarly, to gain insights into the internal dynamics of the system through observation, the system must be observable. It is a recognized fact that a solvable system of linear algebraic equations possesses a solution solely when the system matrix's rank is full. The concepts of controllability and observability are intrinsically linked to rank assessments of specific matrices.

A linear, time-invariant, discrete-time system is considered in the state space described by Equation (2.24), determined through state measurements in the initial state $x(0)$ [31]. The linear discrete-time system is controllable if and only if $\text{Rank}(C_M) = n$, where n is the dimension of vector x and the controllability matrix is defined by

$$C_M = [B \ AB \ A^2B \ \dots \ A^{n-1}B]. \quad (2.27)$$

Similarly, the system is observable if and only if $\text{Rank}(O_M) = n$, where the observability matrix is defined by

$$O_M = \begin{bmatrix} C \\ CA \\ CA^2 \\ \vdots \\ CA^{n-1} \end{bmatrix}. \quad (2.28)$$

This is based on the concept of optimization, and it is performed to minimize a cost function that represents the system's performance as follows:

$$J_{cost} = \int_0^{\infty} (x^T Q x + u^T R u) dt. \quad (2.29)$$

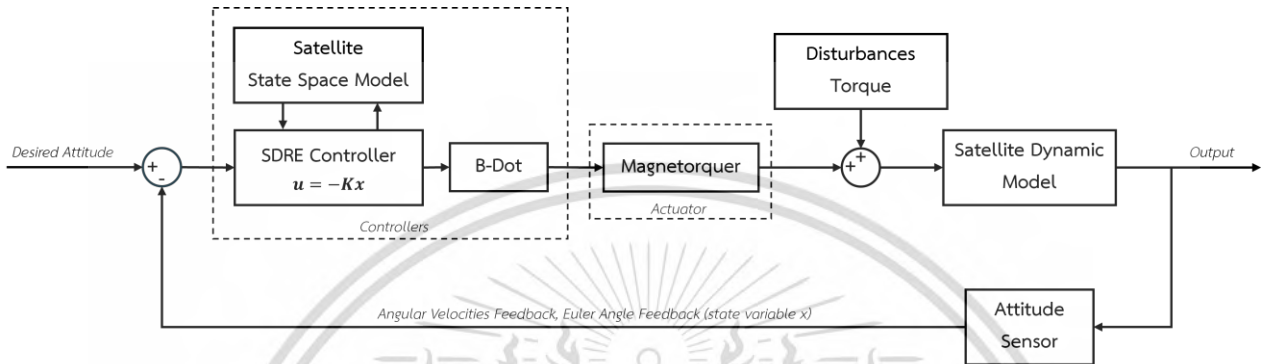


Figure 2.5 The structure of the satellite attitude control system with the SDRE controller

The structure of a satellite attitude control system with an SDRE controller is shown in Figure 2.5. The SDRE approach to acquiring a suboptimal solution for the cost functional J_{cost} and system Equation (2.29) is outlined as follows: Utilize direct parameterization to convert the nonlinear dynamics into the state-dependent coefficient form presented in Equations (2.30)-(2.31) and subsequently solve the associated SDRE provided below.

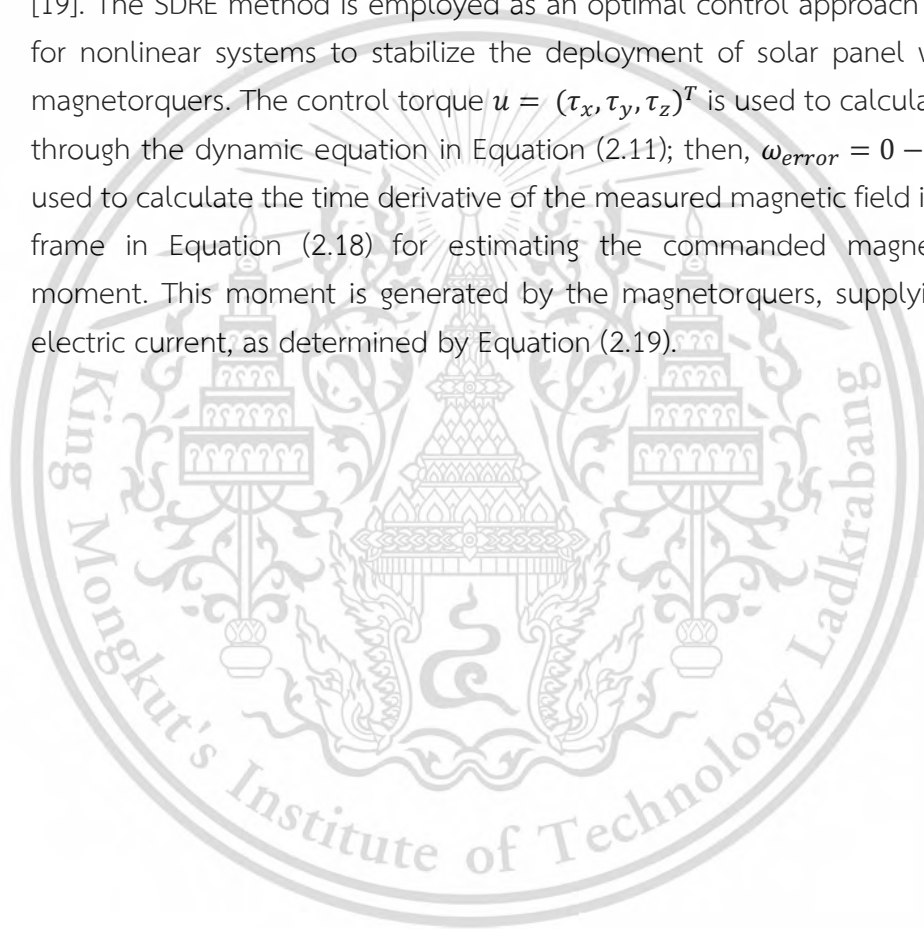
$$A^T P + P A - P B R^{-1} B^T P + Q = 0, \quad (2.30)$$

$$P = Q + A^T (P - P B (R + B^T P B)^{-1} B^T P) A. \quad (2.31)$$

In this context, Q is a positive-definite (or positive-semidefinite) Hermitian or real symmetric matrix, R is a positive-definite Hermitian or real symmetric matrix, and P is determined by solving the Riccati Equations (2.30)-(2.31) using MATLAB.

$$u(t) = -Kx(t) = R^{-1} B^T P x(t). \quad (2.32)$$

Next, a linear feedback controller is constructed using Equation (2.32), where K represents the matrix of the optimal control vector used to validate the de-tumbling along with the pointing control algorithm and stabilization of the solar panel wing deployment of the satellite. In particular, when solar panel wings are deployed on a free-floating space base body, which is treated as a problem of nonholonomic motion planning, the first major task is to successfully stabilize the satellite by adapting to changes in the inertia tensor. The controllability of the spacecraft's base body attitude after the deployment process of solar panel wings can be solved through an optimal control method for nonlinear systems [19]. The SDRE method is employed as an optimal control approach in this task for nonlinear systems to stabilize the deployment of solar panel wings using magnetorquers. The control torque $u = (\tau_x, \tau_y, \tau_z)^T$ is used to calculate $\omega_{control}$ through the dynamic equation in Equation (2.11); then, $\omega_{error} = 0 - \omega_{control}$ is used to calculate the time derivative of the measured magnetic field in the body frame in Equation (2.18) for estimating the commanded magnetic dipole moment. This moment is generated by the magnetorquers, supplying enough electric current, as determined by Equation (2.19).



Chapter 3

Methodology

In this section, the proposed methodology and the approach to compute the satellite's orientation will be introduced. Following that, the models used for characterization and verification will be presented, and finally, the HiLs will be described. To accurately simulate the de-tumbling phase and the post-deployment solar panel phase that occurs in space, a ground-based testing setup requires three main components:

- **Earth's Magnetic Field Environment Simulation:** This apparatus is essential for replicating the Earth's magnetic field environment, which is crucial for creating accurate test conditions. It typically involves the use of a Helmholtz Cage, which generates a controlled and uniform magnetic field, mimicking the geomagnetic conditions encountered by a satellite in orbit.
- **Three-Axis Magnetorquer:** The three-axis magnetorquer is a proposed actuator designed to interact with the simulated Earth's magnetic field environment provided by the Helmholtz Cage. Its primary function is to reduce the satellite's rotation rate by generating the necessary magnetic torques. This is achieved by producing magnetic moments along three orthogonal axes, counteracting the satellite's angular momentum and stabilizing its orientation.
- **Proposed Hardware-in-the-Loop Simulation (HiLs) Platform:** The proposed HiLs platform includes a satellite model and all associated equipment mounted on a mass balance plate, which is designed to float on an air-bearing. This setup allows for dynamic motion with quasi-frictionless rotation, closely simulating the de-tumbling phase experienced in space. The air-bearing system minimizes friction, providing a near-frictionless environment that facilitates accurate testing of the satellite's attitude control and stabilization mechanisms.

These components are described in detail in the following sections.

3.1 Configuration of the Hardware-in-the-Loop Simulation Platform

The HiLs methodology offers an intriguing approach for testing and validating the guidance, navigation, and control software algorithms. It enables on-ground testing, allowing for a thorough assessment and verification of the software's performance.

3.1.1 THREE-AXIS HELMHOLTZ CAGE

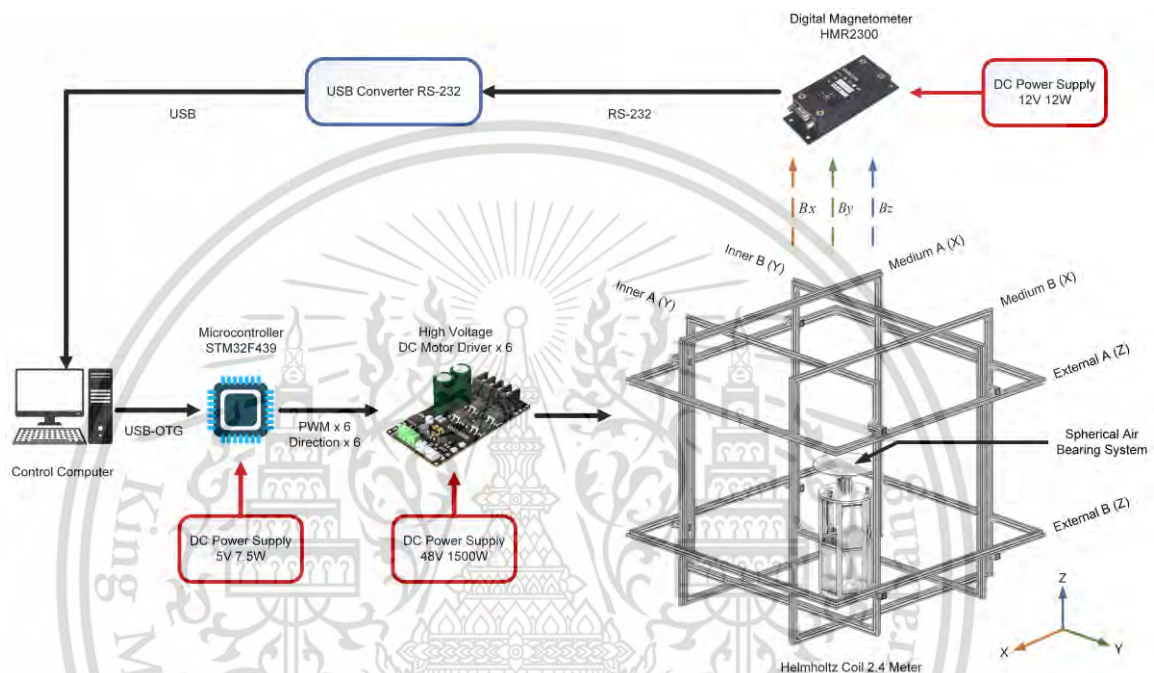


Figure 3.1 A system architecture of proposed HiLs testbed.

For ACS validation, the three-axis Helmholtz cage is the main piece of equipment for generating the EMF based on Biot-Savart's law through a pair of square coils that are arranged coaxially and parallel to one another. The capability of the proposed three-axis square Helmholtz coil can be uniformly formulated as an EMF with 1 ± 0.5 Gauss in a 0.5-meter cubic-like area from the center. Moreover, the boundary parameters of the EMF can also be used to approximate the integral wind-up in the PID controller and guarantee that the control signal does not exceed the capacity of the actuator, which is limited by the wire size. Following the mission requirement, the structural and electrical design of the Helmholtz coil should first be simple to assemble, wind, and bend at the corners. Based on the system architecture shown in Figure 3.1, as a low-level control software, a DC power supply model, TDK-Lambda CUS1500M-48/RF with 48 V and 1500 W, was used to control the voltage sources. Regarding system cooperation, six high-voltage Cytron MD25HV DC motor drives were

This material is reserved for educational use only, not allowed for commercial use.

Forbidden to modify the content, and cite the document when use.

independently used to control the direction and intensity of the magnetic field for each Helmholtz coil via a PWM signal from a 32-bit STM32F439 (NUCLEO-F439ZI model) microcontroller at a speed of 180 MHz sourced by a 5 V low-voltage power supply model, Delta DRC-5V 10W1AZ. High-level control software via C# programming is used to generate the EMF as the command through the SGP4-based satellite orbit propagator and then close-loop feedback on the EMF characteristic by a Honeywell HMR2300 magneto sensor sourced by 12 V, low-voltage power supply model: CUI-Inc.SMM12-1. In summary, the technical specifications of the HiLs are listed in Table 3.1.

Table 3.1 The HiLs testbed sub-system specification.

Sub-systems	Model	Parameters
DC Motor-controller	Cytron MD25HV (6 Pcs.)	Input Voltage: 7-58V Max output current: 25A Output PWM Freq.: 16 kHz
Micro-controller	NUCLEO-F439ZI (1 Pc.)	Model type: ARM Cortex-M4 32-bit Clock Freq.: 180 MHz Flash memory: 2 Mbyte I/O Ports: I/O
Power supply	TDK-Lambda CUS1500M-48/RF (1 Ps.)	Output Voltage: 48V Output Current: 32A Output Power: 1.536kW
	CUI Inc. SMM12-12 (1 Pc.)	Output Voltage: 12V Output Current: 1A Output Power: 12W
Magnetic field sensor	Delta DRC-5V 10W1AZ (1 Pc.)	Output Voltage: 5V Output Current: 1.5A Output Power: 7.5W
	Honeywell HMR2300 (1 Pc.)	Range: ± 2 G Three Axis Digital Output Data Interface: RS232 Sample rate: 10-154 Sam/s

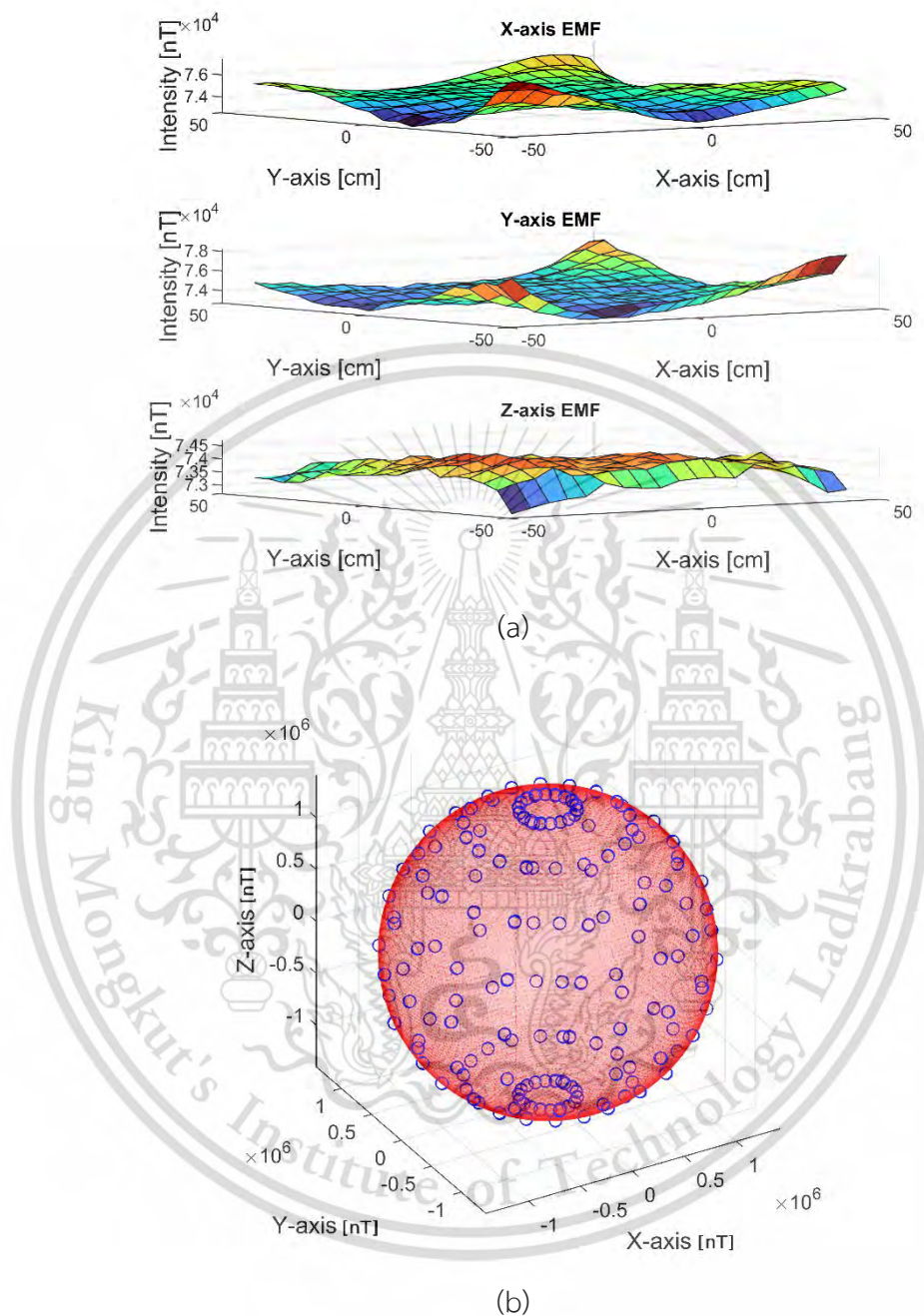


Figure 3.2 Uniformity analysis of the proposed 3D square Helmholtz coil in a one-meter cubic-like area from the center. (a) The original data obtained from the calibrated magnetic sensor were visualized in a 3D surface plot, and (b) the radius of the ellipsoid represents the intensity of the magnetic field, with each transformed coordinate pointing away from the center of the origin

The original data obtained from the calibrated magnetic sensor were visualized in a 3D surface plot, as depicted in Figure 3.2(a). This 3D surface plot demonstrates that the Helmholtz coil can generate a uniform EMF simulation in a one-meter cubic-like area from the center of the cage across all three axes. An ellipsoid fitting model was employed to assess the uniformity of the data, considering the data as a function of elliptical coordinates. In this model, the radius of the ellipsoid represents the intensity of the magnetic field, with each transformed coordinate pointing away from the center of the origin. Ideally, uniformity of the data should result in a spherical shape. This is because the magnetic field generated by the square-shaped Helmholtz coils is expected to be homogeneously distributed at the center of the cage, as shown in Figure 3.2(b). Such a spherical shape is suitable for the microsatellite attitude control system algorithm [9]. The outcome of this sphere test demonstrates that our Helmholtz cage produces a magnetic field that is uniform within a 1-cubic-meter volume. This result helps us understand where to place the satellite model to obtain the most uniform EMF for testing. However, if the data have any biases or irregularities, the fitting model may yield an eccentric shape, deviating from a perfect sphere. This can be caused by localized variations or inconsistencies present in specific regions of the data.

The developed 2.4-meter square Helmholtz coils are capable of generating homogeneous EMF simulation in three axes for functional testing on the ground with low-cost components. The HiLs can achieve an outcome because it is capable of generating EMF simulation under a range of 1 ± 0.5 Gauss and uniformity within a one-meter cubic-like area from the center of the cage, which is initially suitable for performing HiLs for attitude control on the ground for microsatellites in de-tumbling mode via the B-Dot control algorithm.

Table 3.2 Magnetorquer Parameters

Parameters	Value
Dimensions [mm]	200×200×10
Number of turns	250
AWG22 Copper wire diameter [mm]	0.6426
Effective area [m ²]	3.497×10^{-2}
Resistance	9.7
Maximum magnetic dipole moment @ 0.92 A [Am ²]	8.19
Mass [g/Unit]	637.8

This material is reserved for educational use only, not allowed for commercial use.

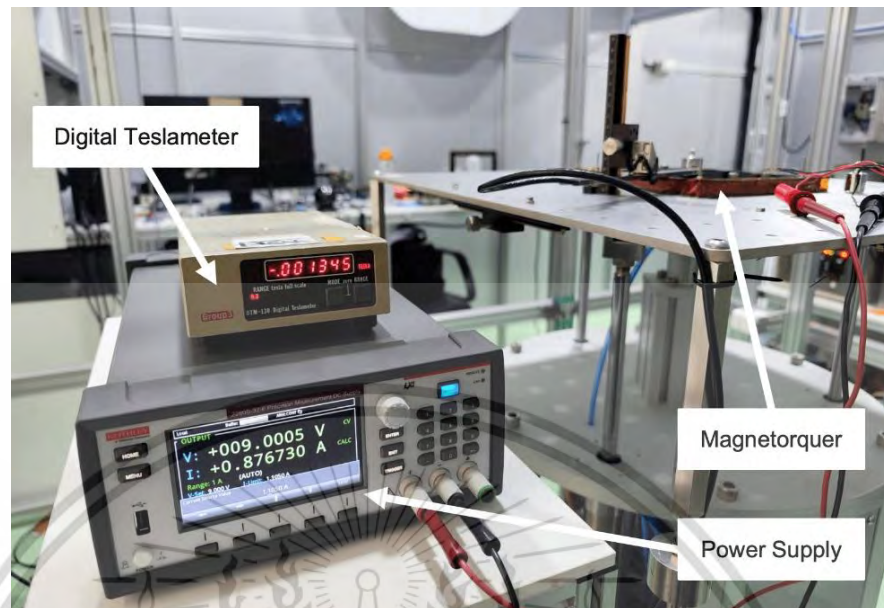


Figure 3.3 The magnetic field of the magnetorquer was measured using a Group3 DTM-130 digital teslameter with an LPT-130 probe and supplied power of 0 V to 15 V.

3.1.2 THE PROPOSED MAGNETORQUER MODEL

Three-axis square air-core magnetorquers have been designed, and the relevant characteristic parameters of these actuators are detailed in Table 3.2. To ensure accuracy, the proposed technique involves computing the magnetic field intensity of the magnetorquer using Biot-Savart's law, as shown in Equation (2.15). The percentage difference in the magnetic field intensity is assessed by comparing the calculated magnetic field intensity with the measured values using Equation (2.16). The variable z ranges from 0 to 120 mm in increments of 10 mm, as defined for this particular task, and a_{sq} is measured at 93.5 mm. To validate the calculations, a Group3 DTM-130 digital teslameter with an LPT-130 probe is utilized. The magnetorquers are supplied with a power voltage ranging from 0 V to 15 V in increments of 0.5 V to measure the actual magnetic field received (b_{mea}), as depicted in Figure 3.3. The validation results of the magnetorquer model accuracy are presented in Figure 3.4(a), which displays a 3D surface plot illustrating the relationship between the measured magnetic field and the measuring point distance on the z -axis of the magnetorquer model. The magnetic field is measured across a range of supplied power voltages from 0V to 15V. Additionally, Figure 3.4(b) shows the magnetic field intensity error of the magnetorquer.

This material is reserved for educational use only, not allowed for commercial use.

Forbidden to modify the content, and cite the document when use.

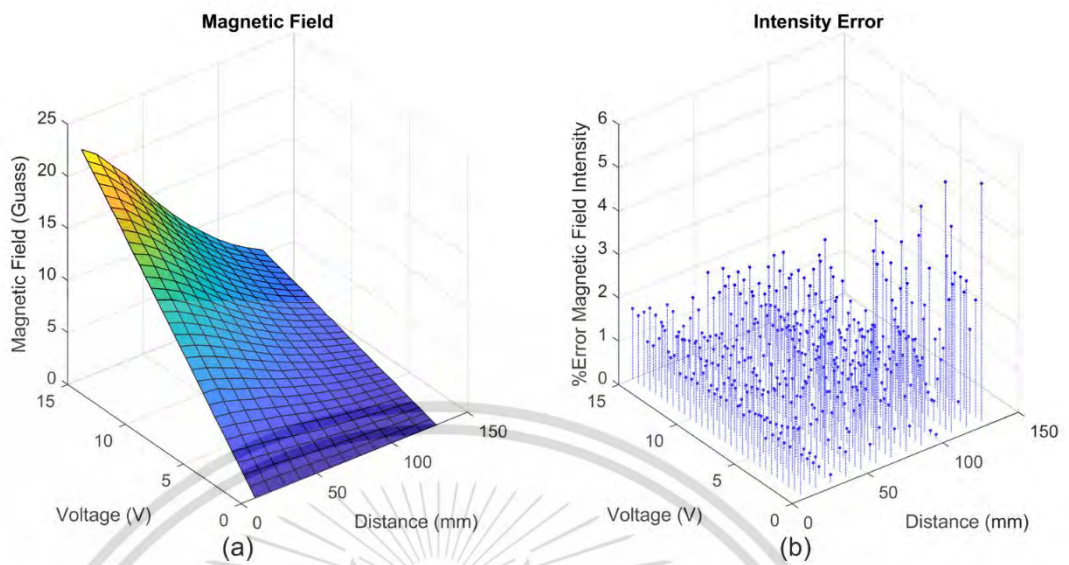


Figure 3.4 (a) A 3D surface plot relationship between the measured magnetic field, and (b) the magnetic field intensity error of the magnetorquer.

Upon analyzing the results, it is observed that the average percentage difference of the magnetic field intensity between the calculated and measured values at the measuring point distances ranging from 0 to 120 mm with 10 mm increments is 1.26%. Notably, the intensity of the measured magnetic field is influenced by the length of the measuring point, with a decrease observed at greater distances. Notably, the designed magnetorquer, equipped with a copper coil AWG22 and operating at a limited current of 0.92 A, can generate a maximum magnetic moment of 8.19 Am^2 . This magnetic moment is sufficient to generate the required torque for de-tumbling the satellite model during the HiLs testing.

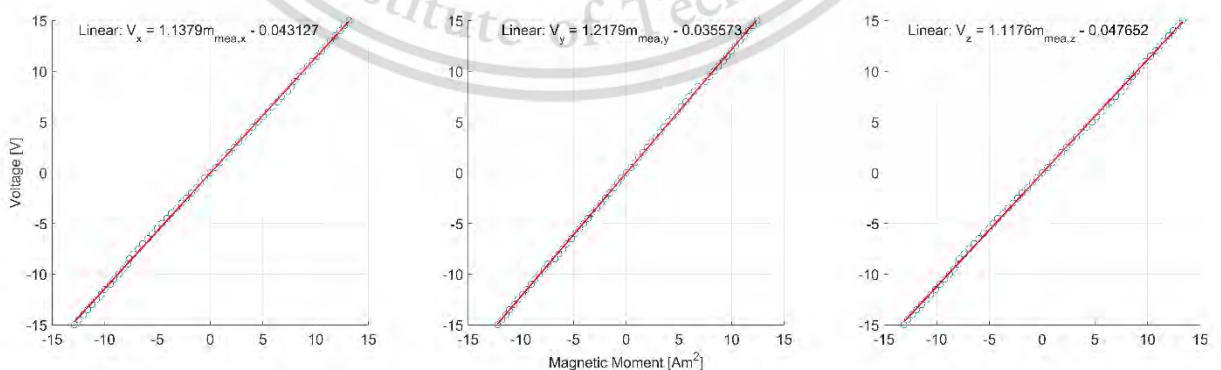


Figure 3.5 Linear approximation of the relationship between the generated magnetic moment and the applied voltage.

This material is reserved for educational use only, not allowed for commercial use.

Forbidden to modify the content, and cite the document when use.

To calibrate the magnetorquers, the relationship between the generated magnetic moment and the applied voltage is determined, as shown in Figure 3.5. Each of the magnetorquers follows the form described in Equation (3.1) for the linear approximation of the calibration curves. These equations are then employed in the control algorithm. Upon receiving the magnetic moment command from the B-Dot controller in Equation (2.19), the system supplies sufficient voltage $(V_x, V_y, V_z)^T$ to each of the magnetorquers for de-tumbling, pointing control, or attitude stabilization in HiLs testing.

$$\begin{aligned} V_x &= 1.1379m_{mea,x} - 0.043127 \\ V_y &= 1.2179m_{mea,y} - 0.035573 \\ V_z &= 1.1176m_{mea,z} - 0.047652 \end{aligned} \quad (3.1)$$

3.1.3 THE PROPOSED HiLs PLATFORM

The proposed HiLs platform serves as a simulation environment for the de-tumbling phase, enabling the validation of the attitude control algorithm using a magnetic field. It utilizes an air-bearing platform that facilitates quasi-frictionless rotational motion to simulate dynamics as if the system were in space. This involves achieving rotational motion free from friction by incorporating air bearings and minimizing the impact of gravitational forces. The latter can be addressed by adjusting the center of mass to align with the system's axis of rotation [32]. In unfortunate circumstances, the center of mass of the testing system cannot be obtained directly but needs to be calculated. Therefore, it is necessary to measure the position of the center of mass through its dynamic characteristics, with relationships defined by equations of motion in Equation (3.2).

$$\Sigma \tau_o = I\alpha = r \times Mg \quad (3.2)$$

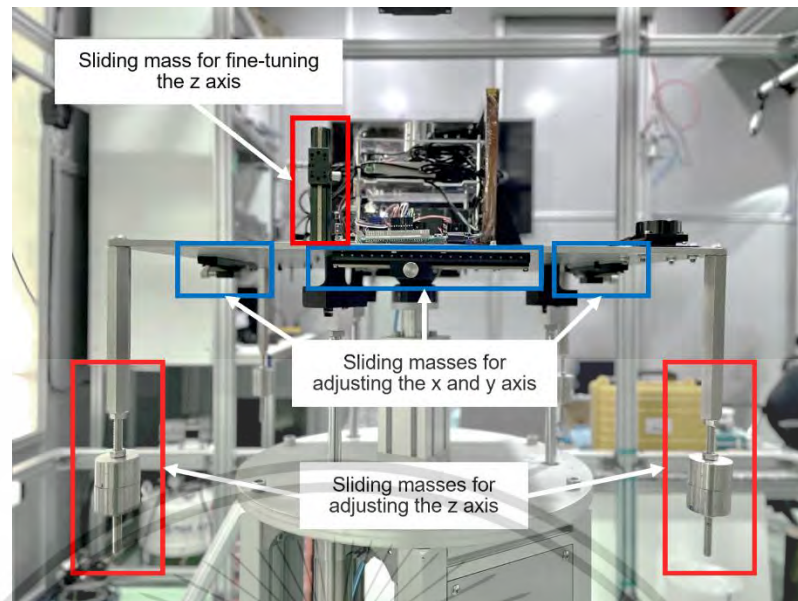


Figure 3.6 The sliding masses for adjusting to balance the satellite system model.

where τ_o represents the external torque due to the gravitational torque, r is the distance from the center of rotation to the center of mass, M is the total mass of the testing system, g is the acceleration due to gravity, I is the inertia tensor of the satellite system model $diag(0.7264, 0.7258, 1.1644)$, and α is the angular acceleration referenced to the coordinate system of the testing system. This is achieved by installing sensors to measure conditions and adjusting masses for balancing the satellite system model on air bearings in the three axes (X, Y, and Z), as illustrated in Figure 3.6. The motion characteristics after adjusting the sliding mass differ due to the position of the center of mass. The results from adjusting the distance of the sliding masses to bring the center of mass closer to the center of rotation by sliding masses are moving in three axes, relocating the center of mass closer to the center of rotation (the geometrical center of the air-bearing mass). The process is repeated until the threshold limit is reached (0.1 mm), as shown in Table 3.2. The sliding masses are adjusted to bring the center of mass closer to the center of rotation. After six iterations, the system achieves balance with $r = (0.025, -0.110, -0.072)$, as shown in Figure 3.7. This balanced configuration is then used for simulating the de-tumbling phase.

Table 3.3 The distance from the center of mass to the center of rotation, adjusted by the sliding masses on the satellite system model to align with the system's axis of rotation.

Iterations of adjusting	The distance r in three axes (X, Y, Z) [mm]
Iteration 1	(0.188, -0.083, 0.171)
Iteration 2	(-0.015, -0.129, -0.069)
Iteration 3	(-0.360, 0.031, 0.047)
Iteration 4	(-0.037, -0.021, 0.056)
Iteration 5	(0.403, -0.067, 0.115)
Iteration 6	(0.025, -0.110, -0.072)

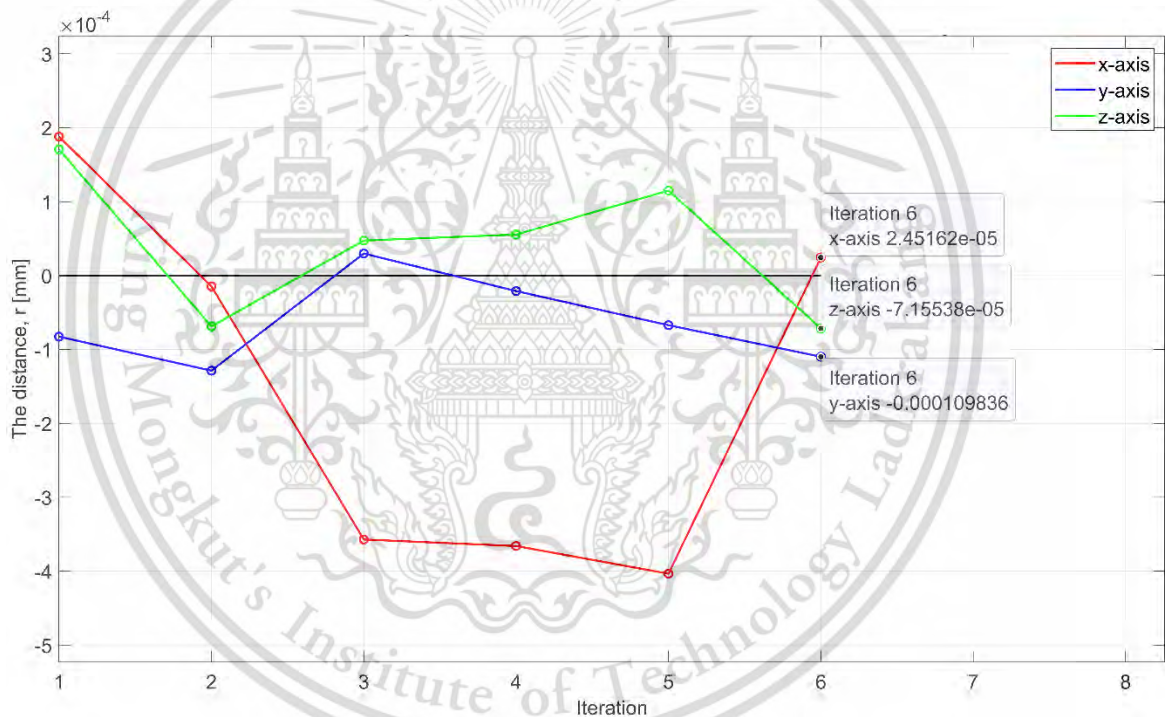


Figure 3.7 The number of iterations required to balance the center of mass to the center of rotation of the satellite system model.

A block diagram representation of the HiLs platform is shown in Figure 3.8. In this setup, the control computer receives attitude data from sensors and the magnetic field command, which is then transmitted to the Helmholtz cage for simulating the EMF. Since the magnetometer is placed near the magnetorquers on the satellite model, it is affected by the magnetic field disturbance generated by the magnetorquers. Therefore, the B-dot algorithm calculates using the command of the EMF that we generate to the Helmholtz cage. This cage has

been proven to produce a magnetic field that is uniform within a 1-cubic-meter volume, and the error that occurs is less than 300 nT in an open environment [9]. The control algorithms implemented in MATLAB are executed, and the resulting driving current data are sent through a Raspberry Pi 4, which functions as a wireless USB hub, to the Arduino Due control board. Subsequently, the voltage commands from the control board are directed to the DC motor drivers responsible for driving the magnetorquers. The magnetorquers generate a magnetic field that interacts with the EMF produced by the Helmholtz cage, ultimately stabilizing the tumbling motion and achieving the desired attitude of the satellite model.

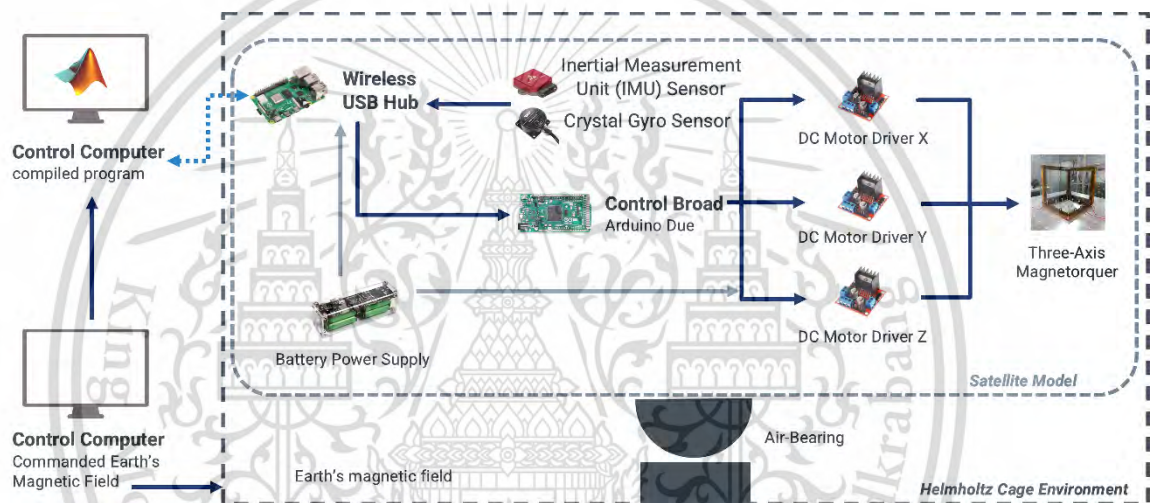


Figure 3.8 Block diagram of the HiLs platform.

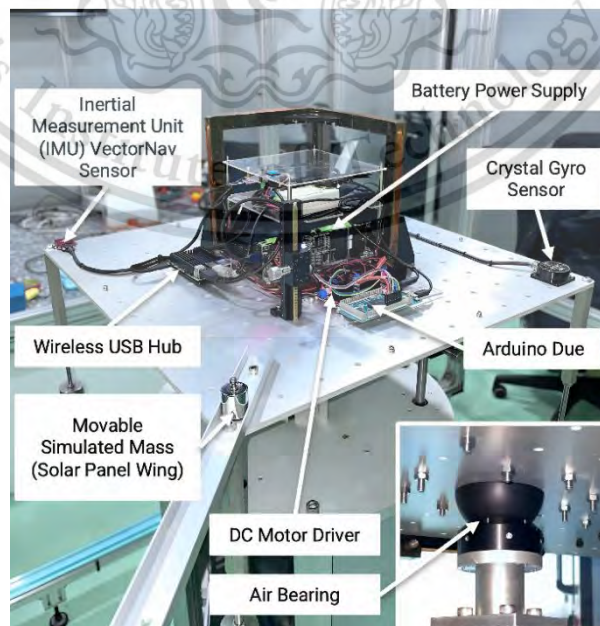


Figure 3.9 The components of the HiLs platform.

This material is reserved for educational use only, not allowed for commercial use.

Forbidden to modify the content, and cite the document when use.

To facilitate current control on the load, the magnetorquers are driven by three L298N DC motor drivers that are capable of providing a maximum current of 2 A with a power output of 25 W. Current control is achieved through pulse width modulation (PWM), where the duty cycle of the command voltage is modulated to regulate the current. Two attitude sensors, namely, the VectorNav VN-100T IMU sensor and the Wit-motion HWT101CT crystal gyro sensor, are employed for measurement purposes. A 160 Wh battery power supply also serves as a voltage source for the wireless USB hub and the DC motor drivers. The components of the HiLs platform are depicted in Figure 3.9.



Chapter 4

Experimental Results

4.1 Experimental Results of De-tumbling along with Pointing Control

In this section, the test scenarios are introduced, utilizing HiLs testing to validate the satellite magnetorquer-based ACS for de-tumbling, along with pointing control in yaw using the B-dot algorithm. This algorithm is designed to investigate the capability and effectiveness of the satellite magnetorquer-based ACS in ground-based testing. The presented scenarios involve control algorithms, employing the cascade PID controller and the optimal SDRE controller. The testing includes the same initial conditions for each controller. To evaluate the de-tumbling control of the magnetorquers, specifically along the yaw axis, an initial condition for yaw rotational motion was established by accelerating the system to achieve a constant angular rate, thus generating torque. Subsequently, the magnetorquer-based ACS of the satellite model initiated the de-tumbling process. In this experimental setup, the constant EMF from the Helmholtz cage, denoted as \vec{b}_{emf} , was set to $\vec{b}_{emf} = (0.226, 0.122, 0.453)$ Gauss, while the initial constant angular rate of the satellite model, represented as ω_{int} , was set to $\omega_{int} = (0, 0, 0.0698)$ rad/s on the air-bearing platform.

Table 4.1 The gain parameters for de-tumbling along with pointing control.

Parameters	Value
B-dot controller gain, k_b	
The cascade PID controller	230, 230, 230
The SDRE controller	3,800, 3,800, 3,800
PI controller gain ($K_{p,ang}, K_{i,ang}$)	$K_{p,ang} = (16, 16, 16)$ $K_{i,ang} = (0.70, 0.80, 0.80)$
PD controller gain ($K_{p,vel}, K_{d,vel}$)	$K_{p,vel} = (0.13, 0.13, 0.11)$ $K_{d,vel} = (0.90, 0.90, 0.70)$
The weighting matrices Q	diag[0.1, 0.1, 0.1, 1, 1, 1]
The weighting matrices R	diag[0.075, 0.075, 0.075]
Inertial properties, I (kgm ²)	diag[0.7264, 0.7258, 1.1644]

In the test scenarios for the cascade PID with the B-dot controller, the B-dot controller gains were set to 230, and the positive gains of the cascade PID controller, including $K_{p,ang}$ and $K_{i,ang}$ for the PI controller and $K_{p,vel}$ and $K_{d,vel}$ for the PD controller. This material is reserved for educational use only, not allowed for commercial use.

controller, were fine-tuned through trial and error to achieve the optimal gains for the satellite model. For the SDRE controller with the B-dot controller tested, the B-dot controller gains were set to 3,800, and the weighting matrices Q and R had only diagonal terms. All the gain parameters in these test scenarios are indicated in Table 4.1.

The angular rate results of the control algorithms are depicted in Figure 4.1, with each axis represented in its own graph. The angular rates for the x , y , and z axes were successfully brought close to their target values, set at $(0, 0, 0)$ rad/s, completing the de-tumbling process in all test cases. The achieved performance metrics for this testing are as follows: for the cascade PID with the B-dot algorithm, the peak time is 354.13 s, the overshoot is 9.16%, and the settling time is within 413.23 s. For the SDRE with the B-dot controller result, the performance metrics consist of settling times of 368.20 s. There is no overshoot.

Figure 4.2 displays the time response of the pointing control from the initial conditions to the desired attitude defined by Euler angles $(\psi, \theta, \phi) = (0, 0, 0)$ deg. Based on the experimental results, for the cascade PID with the B-dot controller, the roll and pitch angles stabilize within 450.00 s in all test cases. In contrast, the yaw angle exhibits an overshoot of 20.92% and reaches a steady state within 600.75 s, reaching 0.27 deg. For the SDRE with the B-dot controller, the roll and pitch angles stabilize within 300.00 s. In comparison, the yaw angle exhibits no overshoot and reaches a steady state within 363.42 sec, reaching -0.18 deg.

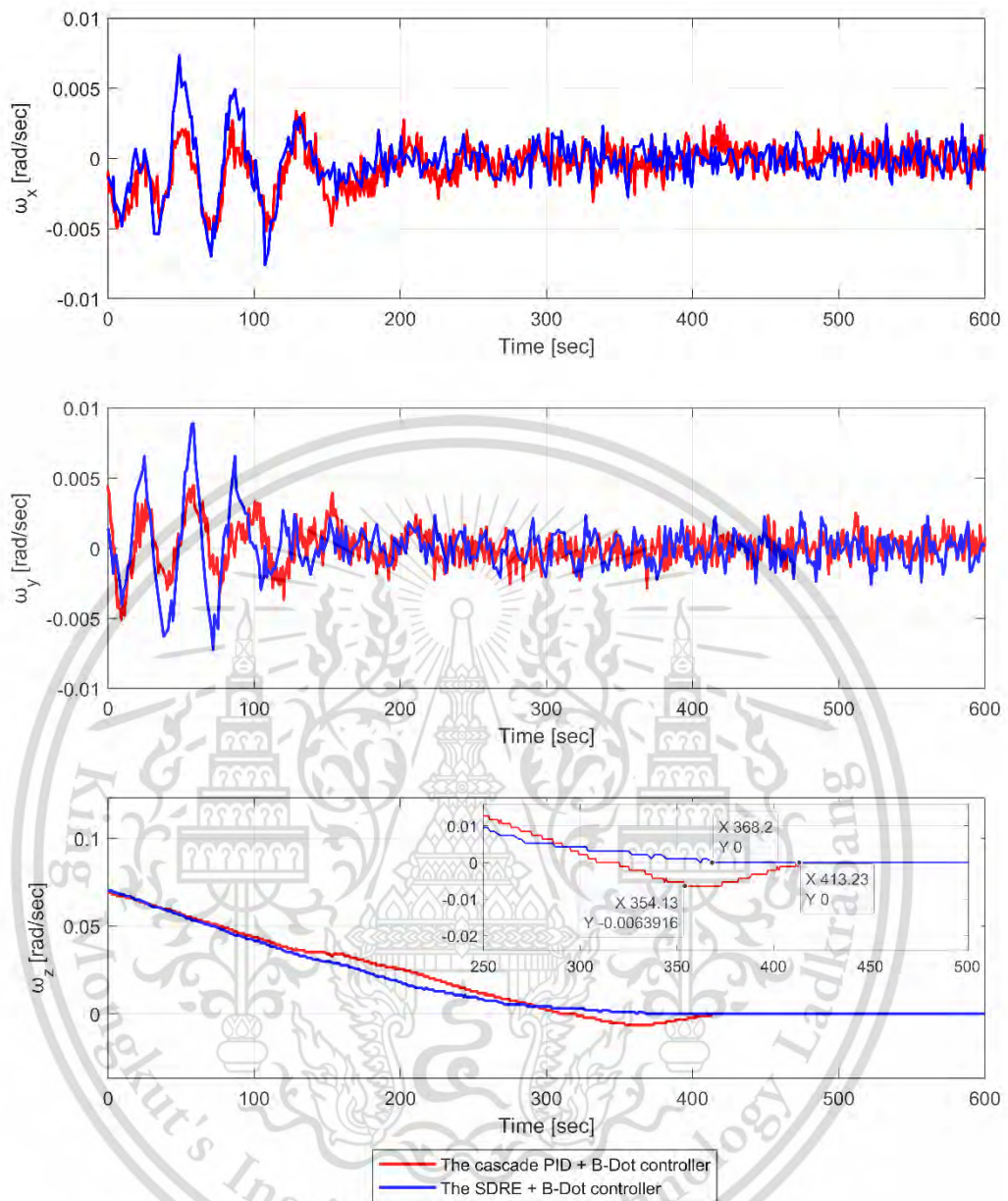


Figure 4.1 The angular rate results of the HiLs test for De-tumbling along with Pointing Control.

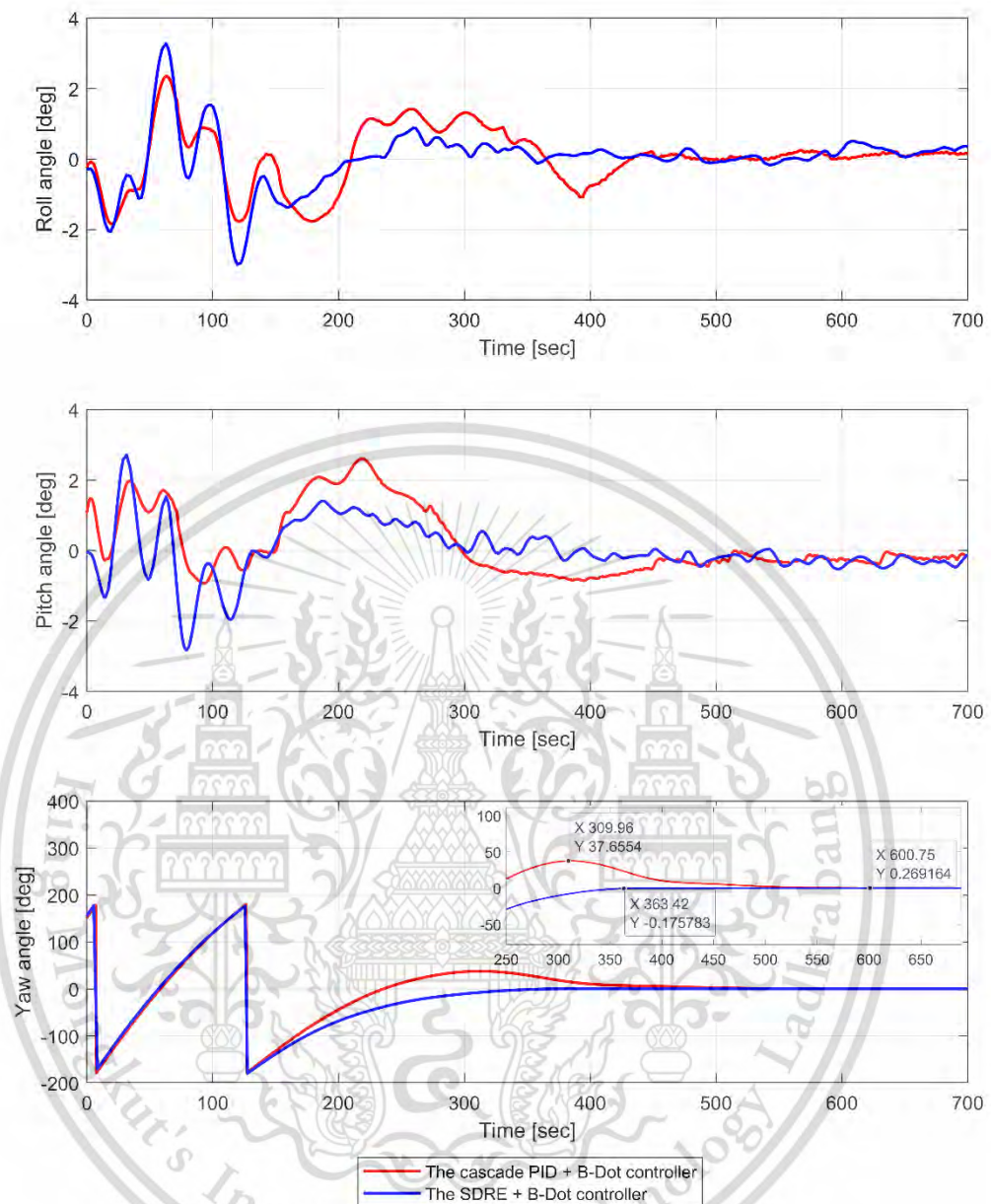


Figure 4.2 The Euler angle results of the HiLs test with for De-tumbling along with Pointing Control.

4.2 Experimental Results of Stabilization After the Deployment of Solar Panel Wings

This experimental SDRE controller is validated for the stabilization of solar wing deployment on a satellite model. This validation serves as proof that this nonlinear optimal control can effectively address the problem of nonholonomic motion planning when solar panel wings are deployed on a free-floating space base body. This test includes three different inertia conditions, along with a single initial condition for

simulating the changes in the inertia tensor when solar panel wings are deployed, which are as follows:

- Test Case 1 (TC1): Stabilization before solar panel wing deployment using inertia I_{TC1} .
- Test Case 2 (TC2): Stabilization after solar panel wing deployment with a change in inertia to I_{TC2} .
- Test Case 3 (TC3): Stabilization after solar panel wing deployment with a change in inertia to I_{TC3} .

Table 4.2 Simulation parameters for HiLs

Parameters	Value
\vec{b}_{emf} [G]	0.226, 0.122, 0.453
ω_{int} [rad/s]	0, 0, 0.0698
Inertial properties (I) [kgm ²]	$I_{TC1} = (0.7264, 0.7258, 1.1644)$ $I_{TC2} = (0.7753, 0.7747, 1.2622)$ $I_{TC3} = (0.8512, 0.8506, 1.4140)$

In this test, we simulate changes in the inertia tensor of the satellite model at three positions. This simulation aims to mimic the effects of deploying solar panel wings, leading to unstable rotation. Subsequently, the control algorithm is validated for stabilization. The simulation parameters and satellite inertial properties for three distinct inertia conditions used in the HiLs test for validating the stabilization of solar panel wings after deployment are detailed in Table 4.2. The outcomes of the SDRE method for stabilization after the deployment of solar panel wings are illustrated in Figure 4.3 and Figure 4.4. For this test scenario, the B-dot controller gains were set to 3,800, and the weighting matrices Q and R included only diagonal terms, as presented in Table 4.1.

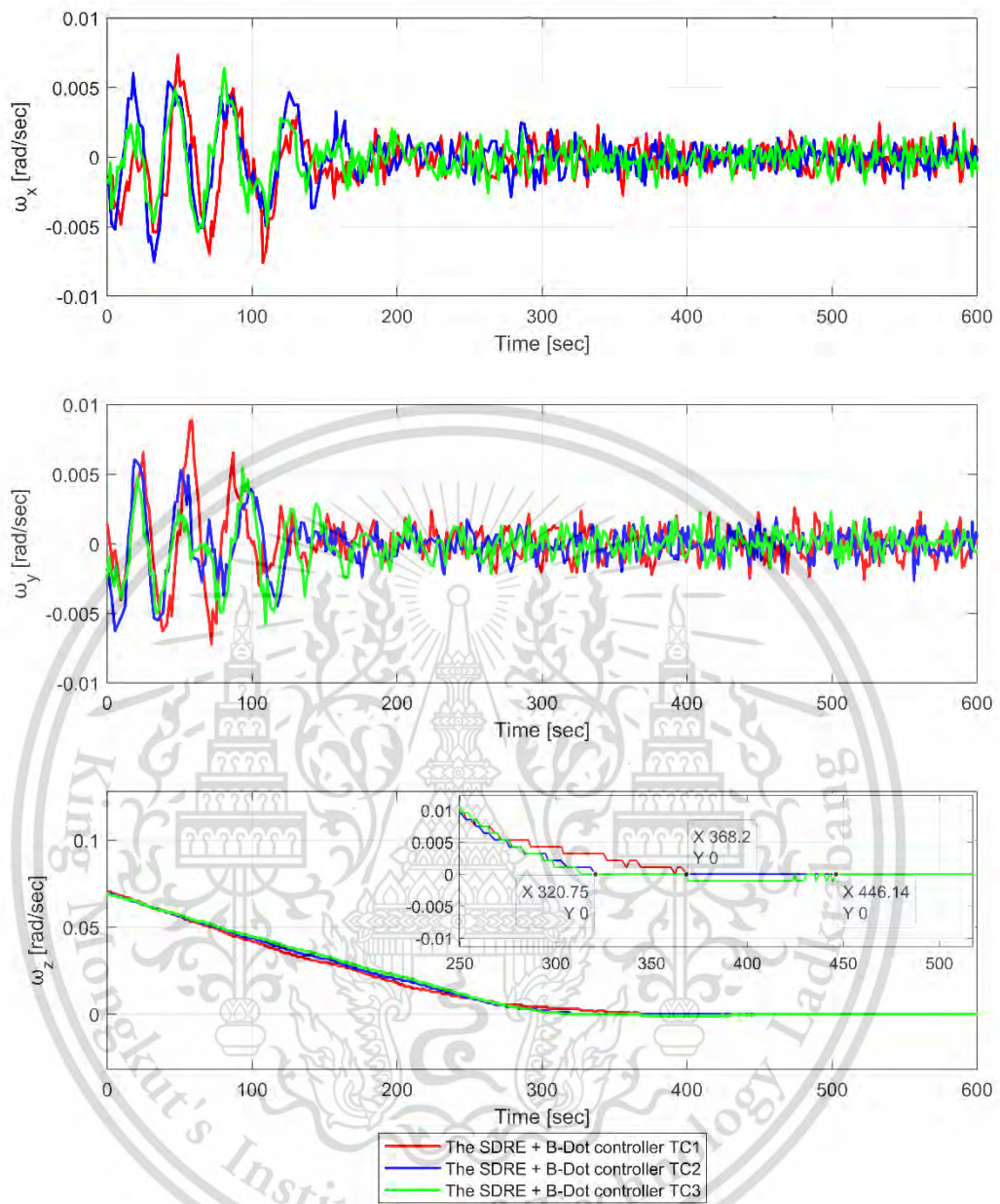


Figure 4.3 The angular rate results of the HiLs test for stabilization after deployment of solar panel wings.

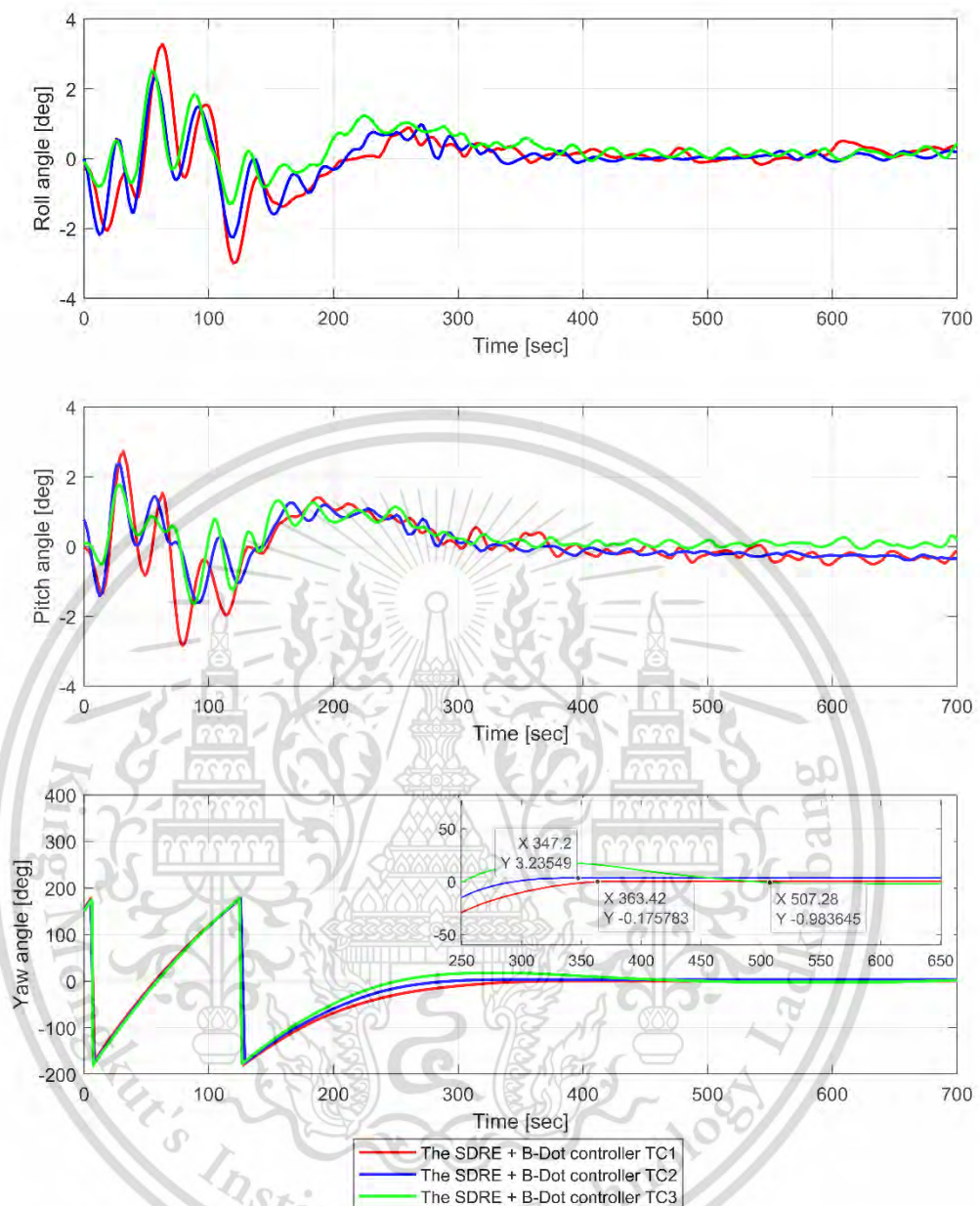


Figure 4.4 The Euler angle results of the HiLs test for stabilization after deployment of solar panel wings.

The time behavior of the angular rates is presented in Figure 4.3, demonstrating the effectiveness of the stabilization after the deployment of solar panel wings in achieving the desired decrease in the angular rates along all three directions. The performance metrics include settling times of 368.20 sec, 320.75 sec, and 486.14 sec for TC1, TC2, and TC3, respectively. Figure 4.4 depicts the behavior of the Euler angles over time for this test scenario. The HiLs are conducted with initial conditions corresponding to the previous test scenario. The experimental results demonstrate that the Euler angles converge to the target values, with the roll and pitch angles

stabilizing within 300.00 sec. In comparison, the yaw angle reaches a steady state within 363.42 sec for TC1, 347.2 sec for TC2, and 507.28 sec for TC3, reaching -0.18 deg, 3.24 deg and -0.98 deg, respectively.

4.3 Discussion

To evaluate the control performance, the step-response characteristics for a dynamic satellite model from the HiLs in each of the three test cases for each control method are summarized in Table 4.3. The first three rows display the results for the cascade PID control method, while the lower three rows show the results for the SDRE control method. The time behavior of the outputs is measured in seconds. From these results, some relevant features of magnetorquer-based ACSs inferred from the HiLs are briefly outlined:

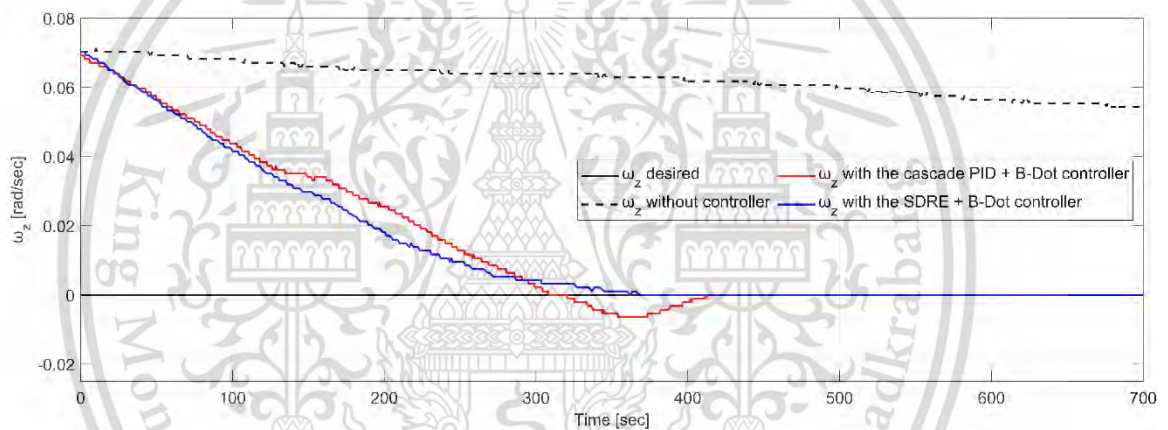


Figure 4.5 The angular rate results with and without the controllers.

- The magnetorquer-based ACS can produce effective de-tumbling and stabilization along with pointing control. The elapsed time that is needed to stabilize, reduce the angular rate and orient the satellite model to the desired attitude is determined. In contrast, the air-bearing satellite model maintains rotation along the z-axis without the control algorithm, as shown in Figure 4.5.
- The pointing accuracy of the magnetorquer-based ACS is acceptable for control operations [33], with a steady-state error lower than ± 5 deg, as shown in Table 4.3. Figure 4.1-4.2 shows a notable difference in the settling time between the SDRE controller and the cascade PID controller for de-tumbling along with pointing control, indicating that the SDRE controller is advantageous. According to both test results in Table 4.3, the cascade PID

controller exhibits overshoot peaks in its output (20.92%) and takes 233.54 sec for rise time and 600.75 sec for settling time to de-tumble along with pointing to reach the desired attitude with the Integral Squared Error (ISE) 0.0590, while the SDRE controller response shows no overshoot peak and takes 334.69 for rise time and 363.42 sec for settling time to de-tumble along with pointing to reach the desired attitude with ISE 0.0745. This indicates that the cascade PID controller displays more aggressive behavior than the SDRE controller. Additionally, fine-tuning all cascade PID controllers for efficient responses can be time-consuming, whereas only two matrices need adjustment in the SDRE controller test cases.

Table 4.3 The evaluation of the de-tumbling along with pointing control performances.

Control Methods	$\Delta\psi_{min}$	$\Delta\psi_{max}$	$\Delta\psi_{mean}$	Overshoot	Rise Time	Settling Time	ISE
The cascade PID	0.14	1.36	1.14	20.92%	233.54	600.75	0.0590
The SDRE	-0.16	0.29	0.07	-	334.69	363.42	0.0745

Table 4.4 The evaluation of the stabilization control performances.

Control Methods		Overshoot	Rise Time	Settling Time	ISE
The SDRE	TC1	-	334.69	363.42	0.0745
	TC2	-	280.48	347.20	0.0996
	TC3	1.54%	243.96	507.28	0.0759

- The evaluation of the stabilization control performance after the deployment of solar panel wings in Table 4.4 shows that under the same initial conditions for each test scenario, there is a notable difference in settling time, giving TC1 and TC2 an advantage over TC3. In all test cases, TC3 exhibits overshoot peaks in its output, while the TC1 and TC2 responses show no overshoot peak. The SDRE controller can stabilize and reach the desired attitude with rise times of TC1 (334.69 sec), TC2 (280.48 sec), and TC3 (243.96 sec), settling times of TC1 (363.42 sec), TC2 (347.20 sec), and TC3 (507.28 sec), with only slight differences and ISE of TC1, TC2 and TC3 are 0.0745, 0.0996 and 0.0759, respectively. This means that the SDRE controller can automatically adjust its control gains to accommodate changes in the system's inertia parameters and dynamics, enhancing its robustness in uncertain environments.

Chapter 5

Conclusion

The experimental results of this testing have been documented. The B-dot algorithm, in conjunction with both the cascade PID controller and the SDRE controller, successfully de-tumbles the satellite model and aligns it with the desired attitude in three test cases, characterizing and verifying the satellite magnetorquer-based ACS. These test cases stabilize after solar panel wing deployment with a change in inertia. Satellite magnetorquer-based ACSs utilizing three-axis magnetorquers have undergone development and testing via HiLs for de-tumbling along with pointing control and attitude stabilization. This comprehensive testing comprises a Helmholtz cage, an EMF in orbit, an air bearing that facilitates quasi-frictionless rotational motion, a satellite system model that balances the center of mass close to the center of rotation, and an onboard computer. Subsequently, the control algorithms employing both the cascade PID controller and the SDRE controller are verified. The experimental results confirm the crucial testing capability of the magnetorquer-based ACS and exhibit a strong correlation with the HiLs results across all test cases. Both the cascade PID controller and the SDRE controller effectively executed de-tumbling control and achieved the desired attitude using a three-axis magnetorquer compared to free rotation without the magnetorquer and controller.

In addition, the experimental results demonstrate that three-axis de-tumbling reduces the angular rate of the satellite model to below 0.0011 rad/s, with a steady-state error of less than 2%. Simultaneously, the pointing control strategy enables the achievement of the desired attitude with an error below ± 5 deg. The time required to stabilize, reduce the angular rate, and orient the satellite model to the desired attitude is 600.75 s for the cascade PID controller. These times are longer than those of the SDRE controller, which are 363.42 s. Additionally, SDRE controllers provide good performance when dealing with satellite dynamic systems, as they can automatically adjust their control gains to accommodate changes in the system's inertia parameters and dynamics from the experimental results of stabilization after deployment of solar panel wings, enhancing their robustness in uncertain environments. The SDRE controller is designed to minimize a quadratic cost function that accounts for both the system's state and control inputs. This approach allows for optimal control of the system by considering its dynamics and constraints.

However, this test only validates the focus of a satellite magnetic-based ACS on the z-axis under constant EMF conditions. Further applications of the HiLs platform are

used to validate the satellite magnetic-based ACS on three axes under EMF simulations by tracking the path of an LEO satellite in the SGP4 orbit and verifying advanced attitude estimation and control strategies using modern control approaches such as model predictive control (MPC). These validations enable the control of nonlinear dynamic systems in the satellite model through the HiLs on-ground testing platform.



This material is reserved for educational use only, not allowed for commercial use.

Forbidden to modify the content, and cite the document when use.

References

- [1] J. N. Pelton and S. Madry, *Handbook of Small Satellites: Technology, Design, Manufacture, Applications, Economics and Regulation: With 476 Figures and 92 Tables*. 2020. doi: 10.1007/978-3-030-36308-6.
- [2] James R. Wertz, *Spacecraft Attitude Determination and Control*, 1st ed., vol. 73. Dordrecht: Springer Netherlands, 1978. doi: 10.1007/978-94-009-9907-7.
- [3] M. Paluszek, *ADCS - Spacecraft Attitude Determination and Control*. 2023. doi: 10.1016/C2021-0-00544-7.
- [4] T. Y. Lin, J. C. Juang, and Vina, "Design and verification of the operating procedure of attitude determination and control subsystem of a nanosatellite," in *CACS 2014 - 2014 International Automatic Control Conference, Conference Digest*, 2014. doi: 10.1109/CACS.2014.7097161.
- [5] E. Silani and M. Lovera, "Magnetic spacecraft attitude control: A survey and some new results," *Control Eng Pract*, vol. 13, no. 3, 2005, doi: 10.1016/j.conengprac.2003.12.017.
- [6] G. Avanzini and F. Giulletti, "Magnetic detumbling of a rigid spacecraft," *Journal of Guidance, Control, and Dynamics*, vol. 35, no. 4, 2012, doi: 10.2514/1.53074.
- [7] R. C. da Silva, R. A. Borges, S. Battistini, and C. Cappelletti, "A review of balancing methods for satellite simulators," *Acta Astronaut*, vol. 187, 2021, doi: 10.1016/j.actaastro.2021.05.037.
- [8] R. C. Da Silva, I. S. K. Ishioka, C. Cappelletti, S. Battistini, and R. A. Borges, "Helmholtz Cage Design and Validation for Nanosatellites HWIL Testing," *IEEE Trans Aerosp Electron Syst*, vol. 55, no. 6, 2019, doi: 10.1109/TAES.2019.2898309.
- [9] J. Chaisakulsurin *et al.*, "Hardware-in-the-Loop Simulation Testbed for Three-Axis Earth's Magnetic Field Generation Based on 2.4- Meter Square Helmholtz Coils," in *2023 IEEE/ION Position, Location and Navigation Symposium, PLANS 2023*, 2023. doi: 10.1109/PLANS53410.2023.10139939.
- [10] S. Chesi, O. Perez, and M. Romano, "A Dynamic, Hardware-in-the-Loop, Three-Axis Simulator of Spacecraft Attitude Maneuvering with Nanosatellite

This material is reserved for educational use only, not allowed for commercial use.

Forbidden to modify the content, and cite the document when use.

- Dimensions A Dynamic, Hardware-in-the-Loop, Three-Axis Simulator of Spacecraft Attitude Maneuvering with Nanosatellite Dimensions,” 2015.
- [11] S. Corpino and F. Stesina, “Verification of a CubeSat via hardware-in-the-loop simulation,” *IEEE Trans Aerosp Electron Syst*, vol. 50, no. 4, 2014, doi: 10.1109/TAES.2014.130370.
- [12] L. Li, J. Yang, X. Shi, and H. Liu, “Robust attitude control for flexible satellite during orbit maneuver,” in *2014 IEEE Chinese Guidance, Navigation and Control Conference, CGNCC 2014*, 2015. doi: 10.1109/CGNCC.2014.7007565.
- [13] M. Lovera and A. Astolfi, “Spacecraft attitude control using magnetic actuators,” *Automatica*, vol. 40, no. 8, 2004, doi: 10.1016/j.automatica.2004.02.022.
- [14] X. Yi and A. Anvar, “Small-satellite magnetorquer attitude control system modelling and simulation,” in *Proceedings - 20th International Congress on Modelling and Simulation, MODSIM 2013*, 2013. doi: 10.36334/modsim.2013.c10.yi.
- [15] V. M. Morozov and V. I. Kalenova, “Satellite Control Using Magnetic Moments: Controllability and Stabilization Algorithms,” *Cosmic Research*, vol. 58, no. 3, 2020, doi: 10.1134/S0010952520030041.
- [16] G. Arantes Jr, A. Santana, and L. Martins-Filho, “Dynamics and control of three-axis satellites by thruster actuators using a linear quadratic regulator,” in *Proc. of International Congress of Mechanical Science*, Brasilia, 2007.
- [17] K. Miyata and J. C. Van Der Ha, “Attitude control by magnetic torquer,” in *Advances in the Astronautical Sciences*, 2009.
- [18] G. Cervettini, S. Pastorelli, H. Park, D. Y. Lee, and M. Romano, “Development and Experimentation of a CubeSat Magnetic Attitude Control System Testbed,” *IEEE Trans Aerosp Electron Syst*, vol. 57, no. 2, 2021, doi: 10.1109/TAES.2020.3040032.
- [19] X. S. Ge, L. Q. Chen, and L. Yan-Zhu, “Optimal control of the deployment process of solar wings on spacecraft,” *Acta Astronaut*, vol. 60, no. 8–9, 2007, doi: 10.1016/j.actaastro.2006.07.020.
- [20] J. Forshaw, “Spacecraft Dynamics and Control: an Introduction A. H. J. de Ruiter et al John Wiley and Sons, The Atrium, Southern Gate, Chichester, West

- Sussex, PO19 8SQ, UK. 2013. 569pp. Illustrated. £62.95. ISBN 978-1-118-34236-7.," *The Aeronautical Journal*, vol. 118, no. 1209, 2014, doi: 10.1017/s0001924000010058.
- [21] F. L. Markley and J. L. Crassidis, *Fundamentals of spacecraft attitude determination and control*. 2014. doi: 10.1007/978-1-4939-0802-8.
- [22] F. L. Markley, "Unit quaternion from rotation matrix," *Journal of Guidance, Control, and Dynamics*, vol. 31, no. 2, 2008, doi: 10.2514/1.31730.
- [23] G. B. Bell and A. A. Marino, "Exposure system for production of uniform magnetic fields," *Electromagn Biol Med*, vol. 8, no. 2, 1989, doi: 10.3109/15368378909020953.
- [24] M. Y. Ovchinnikov, D. S. Roldugin, S. S. Tkachev, and V. I. Penkov, "B-dot algorithm steady-state motion performance," *Acta Astronaut*, vol. 146, 2018, doi: 10.1016/j.actaastro.2018.02.019.
- [25] A. Craig Stickler and K. T. Alfriend, "Elementary magnetic attitude control system," *J Spacecr Rockets*, vol. 13, no. 5, 1976, doi: 10.2514/3.57089.
- [26] A. C. Stickler, "A Magnetic Control System for Attitude Acquisition," 1972.
- [27] K. J. Astrom and T. Hägglund, *Advanced PID control*, vol. 26, no. 1. 2006. doi: 10.1109/MCS.2006.1580160.
- [28] T. Çimen, "State-Dependent Riccati Equation (SDRE) Control: A Survey," *IFAC Proceedings Volumes*, vol. 41, no. 2, 2008, doi: 10.3182/20080706-5-kr-1001.00635.
- [29] F. L. Lewis, D. L. Vrabie, and V. L. Syrmos, *Optimal Control*. Wiley, 2012. doi: 10.1002/9781118122631.
- [30] R. E. Kalman, "On the general theory of control systems," *IFAC Proceedings Volumes*, vol. 1, no. 1, 1960, doi: 10.1016/s1474-6670(17)70094-8.
- [31] R. E. Kalman, "Mathematical Description of Linear Dynamical Systems," *Journal of the Society for Industrial and Applied Mathematics Series A Control*, vol. 1, no. 2, 1963, doi: 10.1137/0301010.
- [32] J. Prado *et al.*, "Three-axis air-bearing based platform for small satellite attitude determination and control simulation," *Journal of Applied Research and Technology*, vol. 3, no. 03, 2005, doi: 10.22201/icat.16656423.2005.3.03.563.

- [33] S. R. Starin and J. Eterno, *Spacecraft Attitude Determination and Control Systems*, vol. 244, no. 3. 2011.



This material is reserved for educational use only, not allowed for commercial use.

Forbidden to modify the content, and cite the document when use.

The logo of Mongkut's Institute of Technology Ladkrabang is a circular emblem. It features a central sunburst with rays emanating from a central point. Below the sunburst are two traditional Thai stupas (chedis) flanking a central decorative element. The entire emblem is surrounded by a circular border containing the text "Mongkut's Institute of Technology Ladkrabang" in a serif font.

Appendix

Experimental Verification of Control Strategies
for Satellite Magnetic-based Attitude Control System
under A Three Axis Helmholtz Cage Environment.

This material is reserved for educational use only, not allowed for commercial use.

Forbidden to modify the content, and cite the document when use.

Experimental Verification of Control Strategies for Satellite Magnetic-Based Attitude Control System Under a Three-Axis Helmholtz Cage Environment

Thanayuth Panyalert^{*†}, Shariff Manuthasna[†], Jormpon Chaisakulsurin[†], Tanawish Masri[†],
Kritsada Palee[†], Pakawat Prasit[†], Peerapong Torteeka[†], Pasu Poonpakdee^{*}, and Poom Konghuayrob^{**‡}

^{*}School of Engineering, Department of Robotics and Artificial Intelligence,
King Mongkut's Institute of Technology Ladkrabang,
No.1, Chalong-Krung, 1-Alley, Ladkrabang, Bangkok 10520, Thailand.

[†]Thai Space Consortium Project, and Center of Observatory Operation and Engineering,
National Astronomical Research Institute of Thailand (Public Organization)
No.260, Don-Kaew, Mae-Rim, Chiang-Mai 50180, Thailand.

[‡]Corresponding author E-mail: poom.ko@kmitl.ac.th

Abstract—During satellite mission planning and operation, the main function of the satellite's attitude determination and control subsystem (ADCS) is to gather information about the satellite's orientation relative to the inertial reference frame. Additionally, this subsystem generates control actions that produce the required torques for adjusting the satellite's orientation, particularly in the context of the Low-Earth Orbit (LEO) regime. This paper focuses on the satellite three-axis attitude control problem for a de-tumbling mode of spacecraft using only magnetorquers as actuators under the presence of noise and investigates their performance through Hardware-in-the-Loop simulation (HiLs) tests, which consisted of a relative Earth's magnetic field generator along with the SGP-4-based satellite orbital propagator high-level control software. The design, development, and verification of proposed satellite attitude control system (ACS) strategies are presented. In detail, as an example of experimentation, the classical B-dot control algorithm is used for the de-tumbling mode to stabilize and reduce the angular rate, along with the pointing algorithm for orienting the satellite to the desired attitude. Then, a cascade Proportional-Integral-Derivative (PID) is implemented to generate enough torque through the three-axis magnetorquers on the frictionless air-bearing platform to verify the performance of the controller using an onboard computer. Finally, the effectiveness of the co-simulation tested as the primary experiment was confirmed through the integrated simulation process.

Index Terms—Satellite Attitude Control System, Three-Axis Magnetorquers, Hardware-in-the-Loop simulation, and Control Strategies.

I. INTRODUCTION

The attitude determination and control subsystem (ADCS) is crucial for ensuring satellite orientation stability and precision when pointing various payloads at specific targets. It comprises two subsystems: Attitude Determination (ADS), which employs sensors to determine the satellite's attitude or angular rates, and Attitude Control System (ACS), which utilizes actuators, control algorithms, and controllers to maneuver the satellite to the desired orientation [1]. The magnetorquer is a form of ACS actuator that generates a magnetic field in order to interact with the Earth's magnetic field (EMF), which is efficient and reliable, especially in low Earth orbit [2]. To prepare the satellite for the nominal mission, the ADCS needs to ensure controllability of its attitude by reducing its initial angular rate and stabilizing

the spinning with high angular rates in the de-tumbling phase of the satellite's attitude after its launch to orbit [3]. For this reason, Hardware-in-the-Loop simulation (HiLs) is an intriguing approach used to test and validate software algorithms for guidance, navigation, and control in a ground-based environment.

The HiLs setup consists of several components. The Helmholtz cage, a crucial device, is capable of simulating the EMF vector experienced by the satellite during its orbital motion. The magnetometer is integrated into the simulation loop to provide feedback on the magnetic field. Additionally, the setup includes an air-bearing platform that facilitates quasi-frictionless rotational motion, essential for simulating the attitude dynamics of the satellite under the control of the magnetic-based ACS [4], [5]. Verifying the satellite process through the HiLs can help save resources, time, and costs. The information given by HiLs assisted the designer in reviewing failure causes and adjusting the control algorithm [6].

In recent years, research on satellite ACS has been fascinating [7]. Linear strategies controllers, such as the PID controller, are utilized; this method is extensively used in ACS and has a simple structure and good stability [8]. Several control techniques have also been approved. However, ground testing, such as HiLs, is still required to continuously improve the performance of the ACS system [9]. Thus, verification and validation of the control strategy through ground-based testing through the HiLs is critical to ensuring that the developed ACS can provide stabilization after deployment. This work primarily focuses on validating the effectiveness of the control algorithm tested through HiLs using a three-axis magnetorquer to de-tumble the satellite model during the de-tumbling phase scenario and verifying the cascade PID controller's performance using an onboard computer.

This paper is organized as follows: The three-axis Helmholtz cage, which is the main equipment of the HiLs architecture, is introduced in Section II. Section III presents the satellite magnetic-based attitude control system methodology, including the attitude dynamics and kinematics, satellite attitude model and control system, magnetorquer model, and

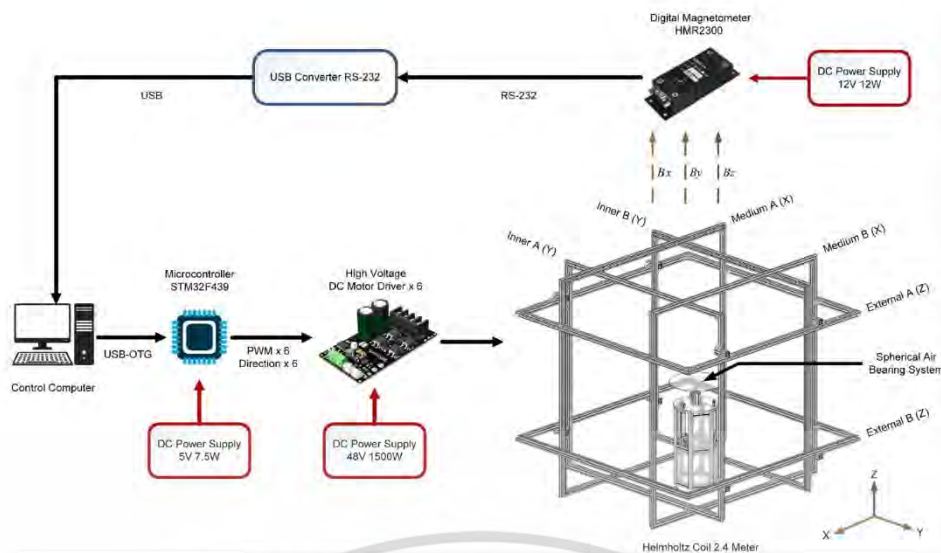


Fig. 1. A system architecture of the proposed HiLs testbed.

HiLs platform. Section IV presents numerical simulations to illustrate the control strategy's effectiveness. Finally, in Section V, the conclusions and future works are presented.

II. HARDWARE-IN-THE-LOOP SYSTEM ARCHITECTURE

A. Three-Axis Helmholtz Cage

The primary equipment used for generating the EMF based on Biot-Savart's law, specifically for ACS validation, is the three-axis Helmholtz cage. This cage consists of a pair of co-axial and parallel square coils. The proposed three-axis square Helmholtz coil has the capability to uniformly generate an EMF of 1 ± 0.5 G within a cubic-like area of 0.5 meters from the center. Furthermore, the boundary parameters of the EMF can also be utilized to estimate the integral wind-up in the PID controller and ensure that the control signal remains within the limits of the actuator, which is restricted by the wire size. In accordance with the mission requirements, the design of the Helmholtz coil should be simple to construct, wind, and bend at the corners. Referring to the system architecture depicted in Figure 1, a DC power supply model, specifically the TDK-Lambda with 48V and 1500W, was employed as the low-level control software. This power supply controlled the voltage sources in coordination with six high-voltage Cytron DC motor drives. Each motor drive was independently responsible for controlling the direction and intensity of the magnetic field for its respective Helmholtz coil using a PWM signal derived from a 32-bit STM32F439 microcontroller running at a frequency of 180 MHz. The microcontroller itself was powered by a 5V low-voltage power supply. The high-level control software, developed using C# programming, is responsible for generating the EMF command. It achieves this by utilizing the SGP4-based satellite orbit propagator. Additionally, the software provides closed-loop feedback on the EMF characteristics using the Honeywell magneto sensor, which is powered by a 12V low-voltage power supply. The detailed technical specifications of the HiLs have been presented in Table 1.

Using affordable components, the square-shaped Helmholtz coils, measuring 2.4 meters, have been developed

TABLE I
THE HILS TESTBED SUB-SYSTEM SPECIFICATION.

Sub-systems	Model	Parameters
DC Motor Drive	Cytron MD25HV (6 Pcs.)	Input Voltage: 7-58 V Max output current: 25A Output PWM Freq.: 16 kHz
Micro-controller	NUCLEO-F439ZI (1 Pc.)	Model type: ARM Cortex-M4 32-bit Clock Freq.: 180 MHz Flash memory: 2 Mbyte I/O Ports: 168 I/O
Power supply	TDK-Lambda CUS1500M-48/RF (1 Pc.)	Output voltage: 48V Output Current: 32A Output Power: 1.536kW
	CUI Inc. SMM12-12 (1 Pc.)	Output voltage: 12V Output Current: 1A Output Power: 12W
	Delta DRC-5V 10W1AZ (1 Pc.)	Output voltage: 5V Output Current: 1.5A Output Power: 7.5W
Magnetic field sensor	Honeywell HMR2300 (1 Pc.)	Range: ± 2 G Three Axis Digital Output Data Interface: RS232 Sample rate: 10-154 Sam/S

to generate a uniform EMF during three-axis functional testing on the ground. The HiLs demonstrates its capability to generate an EMF within a range of 1 ± 0.5 G with uniformity across a one-meter cubic-like area centered within the cage. This feature makes it suitable for conducting ground-based HiLs for attitude control of micro-satellites in de-tumbling mode, utilizing the B-Dot control algorithm.

III. SATELLITE MAGNETIC-BASED ATTITUDE CONTROL SYSTEM METHODOLOGY

A. Magnetic Attitude Dynamics and Kinematics

The magnetic attitude dynamics are modeled by considering the rotation of the spacecraft when using magnetic actuation. The spacecraft is described as a rigid body with

TABLE II
MAGNETORQUER PARAMETERS

Parameter	Value
Dimensions [mm]	200 x 200 x 10
Number of turns	250
AWG22 Copper wire diameter [mm]	0.6426
Effective area [m ²]	3.497 x 10 ⁻²
Resistance	9.7
Maximum magnetic dipole moment @ 0.92 A [Am ²]	8.19
Mass [g]	637.8

independently controlled on each axis. Each air core magnetorquer's magnetic moment is represented by; $m = i \cdot n \cdot A$, where i is the current, n is the number of windings in the coil and A is the area enclosed by a turn of the coil's spiral.

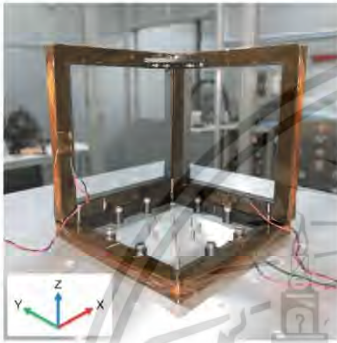


Fig. 3. The three orthogonal magnetorquers.

The percentage difference in the magnetic field intensity given by magnetorquers is verified by comparing the magnetic field intensity between calculating and measuring to confirm the accuracy of magnetorquers. The magnetic field intensity of the magnetorquer m_{mtq} is calculated through Biot-Savart's law in Equation (8),

$$B_{mtq}(z) = \frac{2\mu_0 n i a_{sq}^2}{\pi} \left[(a_{sq}^2 + z^2)^{-1} (2a_{sq}^2 + z^2)^{-\frac{1}{2}} \right], \quad (8)$$

where z is the measure point distance on the z -axis 0 to 120 mm each 10 mm for this task, $\mu_0 = 4\pi \times 10^{-7}$ H/m is the magnetic constant, and a_{sq} is the haft length of the square coil, which is 93.5 mm. The Group3 DTM-130 digital teslameter is used in the validation.



Fig. 4. The magnetic field measurement of the magnetorquer was done using a Group3 DTM-130 digital teslameter and supplied power from 0V to 15V.

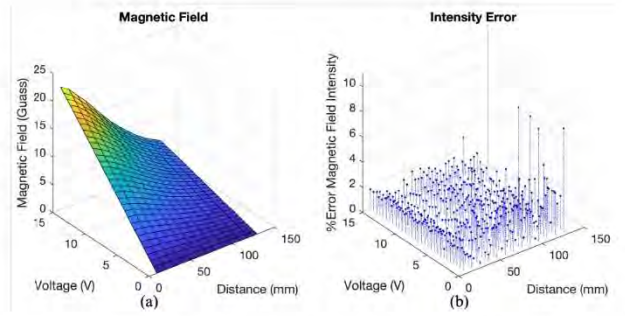


Fig. 5. (a) A 3D surface plot relationship between the measured magnetic field and (b) the magnetic field intensity error of the magnetorquer.

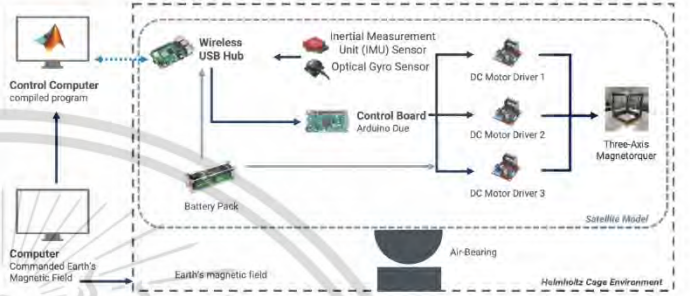


Fig. 6. Block diagram of the HiLs platform.

A power voltage of 0V to 15V is supplied to the magnetorquer at 0.5V to measure the actual magnetic field received (B_{mea}). As shown in Figure 4, the percentage difference of magnetic field intensity (%error) can be defined as follows:

$$\%error = \frac{B_{mtq} - B_{mea}}{B_{mea}} \times 100. \quad (9)$$

The validation result of the magnetorquer model accuracy is described in Figure 5. (a) represents a 3D surface plot relationship between the measured magnetic field from supplied power voltage 0V to 15V and the measuring point distance on the z -axis of the magnetorquer model, and (b) shows the magnetic field intensity error of the magnetorquer. The average percentage difference of magnetic field intensity between calculating and measuring at the measuring point distance on the z -axis of 0 to 120 mm, each 10 mm, is 1.26%. It can be seen that the intensity of the measured magnetic field depends on the measuring point distance. The magnetic field intensity will decrease at a more distant measurement point. The magnetic dipole moment is calculated using Equation (10) below.

$$m_{mea} = \frac{4B_{mea}(z)\pi}{2\mu_0} \left[(a_{sq}^2 + z^2)^1 (2a_{sq}^2 + z^2)^{\frac{1}{2}} \right], \quad (10)$$

where m_{mea} is the measured magnetic dipole moment of the magnetorquer and the maximum magnetic moment of the designed magnetorquer at limited current is 0.92. A copper coil, AWG22, is 8.19 Am², which is enough to generate torque to detumble the satellite model in the HiLs testing.

D. HiLs Platform

The HiLs platform is used to simulate the de-tumbling phase by creating dynamic motions with an air-bearing platform that enables quasi-frictionless rotational motion to

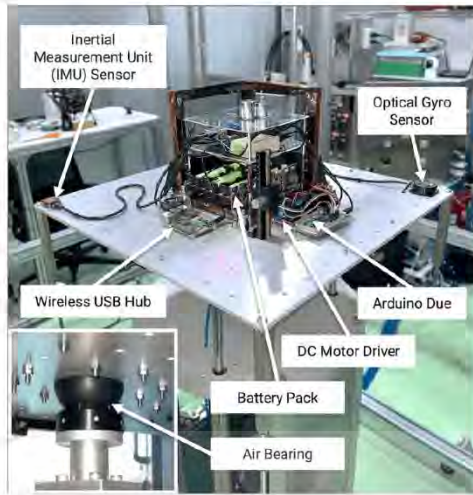


Fig. 7. The components of the HiLs platform.

validate the attitude control algorithm. The HiLs platform is represented in a block diagram in Figure 6.

The control computer obtains attitude data from the sensors as well as the magnetic field command, which is then transmitted to the Helmholtz cage to simulate the EMF. Following that, the control algorithms developed in MATLAB are executed, and the corresponding driving current data is sent through the Raspberry Pi 4, which acts as a wireless USB hub, to the Arduino Due control board. Then the voltage commands from the control board are sent to drive the magnetorquers through DC motor drivers to generate a magnetic field to interact with the EMF from the Helmholtz cage until the satellite model stops tumbling and reaches the desired attitude.

To enable current control on the load, the magnetorquers are powered by three L298N DC motor drivers. These drivers are capable of delivering a maximum current of 2A with a power capacity of 25W. The current control is achieved by utilizing pulse width modulation (PWM) to apply a command voltage to the load. This PWM modulation adjusts the duty cycle of the command, thereby controlling the current flow. Two attitude sensors are used to measure, including the VectorNav VN-100T IMU sensor and the Wit-motion HWT101CT optical gyro sensor, and The battery pack's capacity of 160 Wh is a voltage source for USB hub wireless and DC motor drivers. The components of the HiLs platform are shown in Figure 7.

IV. EXPERIMENTAL RESULTS

In this section, the HiLs testing is used to validate the satellite magnetic-based ACS, and the de-tumbling control in yaw using the B-Dot algorithm with the cascade PID control is designed to investigate the satellite magnetic-based ACS's capability and effectiveness in ground-based testing.

In order to test de-tumbling control of the magnetorquers around the yaw axis, the initial condition for yaw rotational motion was created by accelerating to reach a constant angular rate and produce torque. After that, the satellite magnetic-based ACS starts to de-tumble the satellite model. In this experimental, the constant EMF from Helmholtz cage \vec{B}_{emf} and the satellite model's initial constant angular rate ω_{int}

on air-bearing were set to $\vec{B}_{emf} = (0.226, 0.122, 0.453)^T$ G and $\omega_{int} = (0, 0, 0.0698)^T$ rad/sec, respectively. The B-Dot controller gains of this testing are 100, and the cascade PID positive gains, including ($K_{p,ang}$ and $K_{i,ang}$) of the PI controller and ($K_{p,vel}$ and $K_{d,vel}$) of the PD controller, are tuned by trial and error to find the optimal gains of this satellite model. The simulation parameters and satellite inertial properties for the HiLs testing are indicated in Table 3.

TABLE III
SIMULATION PARAMETERS FOR HiLs

Parameter	Value
\vec{B}_{emf} [G]	0.226, 0.122, 0.453
ω_{int} [rad/sec]	0, 0, 0.0698
Sampling period (T) [sec]	0.05
B-Dot controller gain (k_b)	100, 100, 100
PI controller gain	$K_{p,ang} = (10.5, 10, 9)$ $K_{i,ang} = (0.7, 0.8, 0.9)$
PD controller gain	$K_{p,vel} = (0.14, 0.14, 0.12)$ $K_{d,vel} = (0.6, 0.55, 0.6)$
Inertial properties (J) [kgm ²]	$J = (0.5462, 0.5442, 0.8936)$

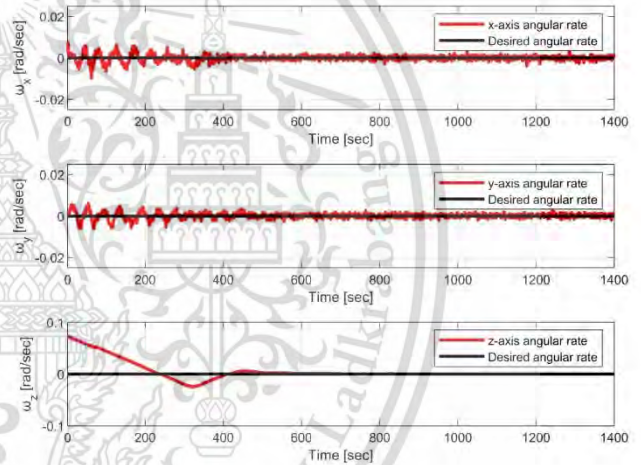


Fig. 8. The angular rate results of the HiLs with the cascade PID controller.

The angular rate results of the control algorithm are shown in Figure 8. The different axes are represented by their own graphs. The angular rate of the x , y , and z axes is settled to the target values (0, 0, 0) rad/sec to complete de-tumbling with 322.26 sec peak time, 33.82% overshoot, and settling time within 568.88 sec at 0.0011 steady state error lower than 2% acceptable.

Figure 9 shows the behavior in time of pointing control in the initial conditions to the desired attitude at Euler angles $(\phi, \theta, \psi) = (0, 0, 0)$ deg. From the experimental results, the roll and pitch angles are stabilized within 450 sec, and the yaw angle settles within 892.43 sec at a steady-state error of 3.58, lower than 2% acceptable.

The experimental results of this testing are represented. The B-Dot algorithm with the cascade PID controller de-tumbles the satellite model and points to the desired attitude. The elapsed time to stabilize, reduce the angular rate and orient the satellite model to the desired attitude is 892.43 sec. In contrast, the satellite model on air-bearing keeps rotation in

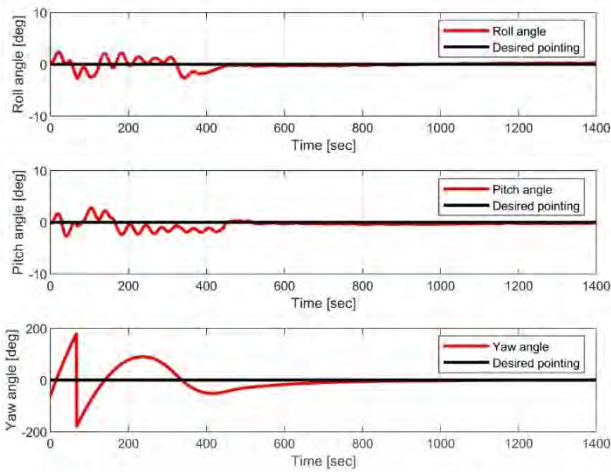


Fig. 9. The Euler angle results of the HiLs with the cascade PID controller.

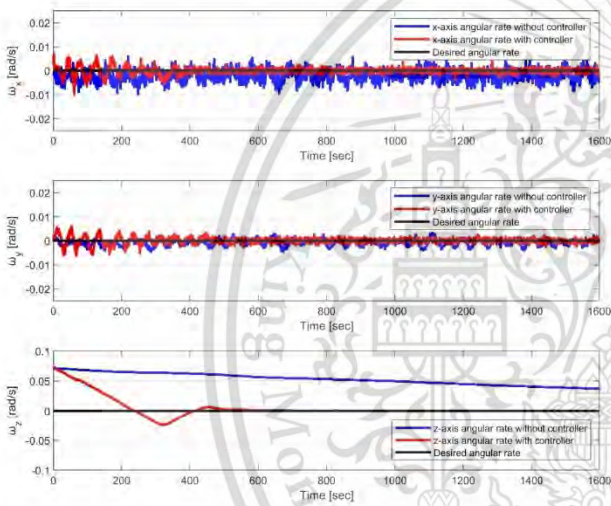


Fig. 10. The angular rate results with and without the control algorithm.

the z-axis without the control algorithm, as shown in Figure 10.

V. CONCLUSION

The satellite magnetic-based ACS using the three-axis magnetorquer has been developed and tested through the HiLs in the de-tumbling phase, including the Helmholtz cage, which simulates the EMF in orbit, the air-bearing, which enables quasi-frictionless rotational motion, and the on-board computer. Then the control algorithm using a cascaded PID controller is verified. The experimental results provide critical testing capabilities for magnetic-based ACS.

The experimental results are well correlated with the HiLs. The cascade PID controller successfully implemented the de-tumbling and pointing control using a three-axis magnetorquer, compared with the free rotation case without the magnetorquer and controller. In addition, the experimental results show that the three-axis de-tumbling reduces the angular rate of the satellite model below 0.0011 rad/sec at a steady-state error lower than 2% acceptable. At the

same time, the pointing control strategy allows reaching the desired attitude with an error below 3.58 deg at steady state and a steady state error lower than 2% acceptable. However, this testing only validates the satellite magnetic-based ACS in the constant EMF. Further applications of the HiLs platform are used to validate the satellite magnetic-based ACS under the EMF simulation by tracking the path of the LEO satellite in SGP4 orbit and verifying the advanced attitude estimation and control strategies validation in modern control approaches such as quadratic regulator controller (LQR) and Model Predictive Control (MPC) to control the nonlinear dynamics system of the satellite model through HiLs on-ground testing platform.

ACKNOWLEDGMENT

Special thanks to the National Research Council of Thailand for their financial support that facilitated the success of our research through the Hub of Talents in Spacecraft Scientific Payload, Grant No. N35E660131, and the Hub of Knowledge in Space Technology and its Application, Grant No. N35E660132. Moreover, we also wish to acknowledge the PBP CMU Electron Linac Laboratory (PCELL) at the Plasma and Beam Physics Research Facility of Chiang Mai University, Thailand, which supports the measuring equipment to validate the magnetic actuator in this experiment.

REFERENCES

- [1] J. N. Pelton and S. Madry, *Handbook of Small Satellites: Technology, Design, Manufacture, Applications, Economics and Regulation*. Springer, 2020.
- [2] E. Silani and M. Lovera, "Magnetic spacecraft attitude control: a survey and some new results," *Control engineering practice*, vol. 13, no. 3, pp. 357–371, 2005.
- [3] G. Avanzini and F. Giuliotti, "Magnetic detumbling of a rigid spacecraft," *Journal of guidance, control, and dynamics*, vol. 35, no. 4, pp. 1326–1334, 2012.
- [4] J. Chaisakulsurin, S. Manuthasna, T. Masri, T. Panyalert, K. Palee, P. Prasit, P. Kamsing, and P. Torteeka, "Hardware-in-the-loop simulation testbed for three-axis earth's magnetic field generation based on 2.4-meter square helmholtz coils," in *2023 IEEE/ION Position, Location and Navigation Symposium (PLANS)*, 2023, pp. 829–834.
- [5] R. C. da Silva, F. S. K. Ishioka, C. Cappelletti, S. Battistini, and R. A. Borges, "Helmholtz cage design and validation for nanosatellites hwl testing," *IEEE Transactions on Aerospace and Electronic Systems*, vol. 55, no. 6, pp. 3050–3061, 2019.
- [6] S. Corpino and F. Stešina, "Verification of a cubesat via hardware-in-the-loop simulation," *IEEE Transactions on Aerospace and Electronic Systems*, vol. 50, no. 4, pp. 2807–2818, 2014.
- [7] L. Li, J. Yang, X. Shi, and H. Liu, "Robust attitude control for flexible satellite during orbit maneuver," in *Proceedings of 2014 IEEE Chinese Guidance, Navigation and Control Conference*. IEEE, 2014, pp. 2531–2536.
- [8] X. Yi and A. Anvar, "Small-satellite magnetorquer attitude control system modelling and simulation," 2013.
- [9] G. Cervellini, S. Pastorelli, H. Park, D. Y. Lee, and M. Romano, "Development and experimentation of a cubesat magnetic attitude control system testbed," *IEEE Transactions on Aerospace and Electronic Systems*, vol. 57, no. 2, pp. 1345–1350, 2020.
- [10] H. D. Curtis, *Orbital mechanics for engineering students*. Butterworth-Heinemann, 2013.
- [11] M. C. Mahdi, *Attitude stabilization for CubeSat: concepts and technology*. Cambridge Scholars Publishing, 2018.
- [12] J. R. Wertz, *Spacecraft attitude determination and control*. Springer Science & Business Media, 2012, vol. 73.
- [13] H. Schaub and J. L. Junkins, *Analytical mechanics of space systems*. Aiaa, 2003.
- [14] Y. Yang, *Spacecraft modeling, attitude determination, and control: quaternion-based approach*. CRC Press, 2019.
- [15] F. L. Markley and J. L. Crassidis, *Fundamentals of spacecraft attitude determination and control*. Springer, 2014, vol. 1286.

Author Biography

Full Name: Mr. Thanayuth Panyalert
 Date of Birth: 21 October 1992, in Chiang Mai
 Address: 16/4 Village No. 4, Muang Pee Nong,
 Ma Khun Whan,
 San Pa Tong, Chiang Mai, 50120,
 Call. 08-3914-5398.



Education: 2015 Bachelor of Engineering in
 Mechanical Engineering,
 Chiang Mai University.

Skills: 1.) Spacecraft Dynamic System.
 2.) Satellite Magnetic-Based Attitude Control Systems.

Experiences and Research Results:

2015-2021: Operation Engineer at Gulf JP NK2 Company Limited.
 - Fouling Monitoring of Plate Heat Exchanger.

2021-2023: Assistant Researcher at National Astronomical Research Institute
 of Thailand (NARIT).
 - Hardware-in-the-Loop Simulation Testbed for Three-Axis Earth's
 Magnetic Field Generation Based on 2.4- Meter Square
 Helmholtz Coils.
 - Experimental Verification of Control Strategies for Satellite
 Magnetic-based Attitude Control System under A Three Axis
 Helmholtz Cage Environment.

Present: Mechanical and System Engineer at National Astronomical
 Research Institute of Thailand (NARIT).